**Alma Mater Studiorum - Università di Bologna**

---

Scuola di Ingegneria
Dipartimento di Ingegneria dell'Energia Elettrica e
dell'Informazione "Guglielmo Marconi"

*Tesi di Laurea Magistrale*
*in*
Communication Systems: Theory and Measurements M

# Multi-mode Communications in Near Field exploiting OAM properties

Candidata:
**Giulia Torcolacci**

Relatore:
**Prof. Ing. Davide Dardari**

Correlatori:
**Dott. Ing. Nicolò Decarli**
**Ing. Marina Lotti**

---

Sessione II
Anno Accademico 2021-2022

# Abstract

This dissertation analyzes the exploitation of the orbital angular momentum (OAM) of the electromagnetic waves with large intelligent surfaces in the near-field region and line-of-sight conditions, in light of the holographic MIMO communication concept.
Firstly, a characterization of the OAM-based communication problem is presented, and the relationship between OAM-carrying waves and communication modes is discussed. Then, practicable strategies for OAM detection using large intelligent surfaces and optimization methods based on beam focusing are proposed. Numerical results characterize the effectiveness of OAM with respect to other strategies, also including the proposed detection and optimization methods.
It is shown that OAM waves constitute a particular choice of communication modes, i.e., an alternative basis set, which is sub-optimum with respect to optimal basis functions that can be derived by solving eigenfunction problems. Moreover, even the joint utilization of OAM waves with focusing strategies led to the conclusion that no channel capacity achievements can be obtained with these transmission techniques.

# Contents

1 **Introduction** 1

2 **Communication with Large Intelligent Surfaces** 3
  2.1 Communication Modes . . . . . . . . . . . . . . . . . . . . . . . 5
  2.2 Optimal communication modes with circular LISs . . . . . . . . 7

3 **Orbital Angular Momentum** 10
  3.1 General Definition . . . . . . . . . . . . . . . . . . . . . . . . . 10
  3.2 State of The Art . . . . . . . . . . . . . . . . . . . . . . . . . . 13
  3.3 Experimental Validations and Contributions . . . . . . . . . . . 15
  3.4 Interpretation . . . . . . . . . . . . . . . . . . . . . . . . . . . 17

4 **OAM-based Communication using LISs** 20
  4.1 Focused OAM . . . . . . . . . . . . . . . . . . . . . . . . . . . . 22
  4.2 Uncoded Transmissions on AWGN channels . . . . . . . . . . . 24
  4.3 Strategies for System's Complexity Reduction . . . . . . . . . . 29
    4.3.1 Accumulation . . . . . . . . . . . . . . . . . . . . . . . . 29
    4.3.2 Smart Integration . . . . . . . . . . . . . . . . . . . . . . 32
    4.3.3 Energy Detection . . . . . . . . . . . . . . . . . . . . . . 34

5 **Numerical Study** 39
  5.1 Simulation Setup . . . . . . . . . . . . . . . . . . . . . . . . . . 39
  5.2 Received EM Field . . . . . . . . . . . . . . . . . . . . . . . . . 40
  5.3 Degrees of Freedom . . . . . . . . . . . . . . . . . . . . . . . . . 44
  5.4 Performance in AWGN . . . . . . . . . . . . . . . . . . . . . . . 49
  5.5 Discussion . . . . . . . . . . . . . . . . . . . . . . . . . . . . . . 52

6 **Conclusion** 55

# Chapter 1

# Introduction

The ceaseless quest for high-speed, reliable, and ubiquitous wireless services is leading today's radio networks to their utmost. Fifth-generation (5G) wireless networks, exploiting the most advanced radio technologies, e.g., multiple-input multiple-output (MIMO) communications, have already been deployed in many countries and are establishing themselves as essential techniques to manage the ever-increasing number of devices' connections. However, it is foreseen that sixth-generation (6G) wireless networks will push these requirements to the ultimate limit of the wireless channel, introducing even more stringent requisites regarding user throughput, latency, scalability, and reliability, paving the way for massively novel applications and use cases.

In this framework, the exploitation of higher operating frequencies, where a more considerable amount of spectral resources is available, in conjunction with the usage of large antenna arrays and antennas densification, has been envisaged as a potential, beneficial approach to tackle the challenging prerequisites that have been outlined.

Nevertheless, the adoption of millimeter-wave communications and terahertz technologies entails larger path losses, susceptibility to atmospheric turbulences, and in some cases, failure of traditional electromagnetic (EM) propagation models based on far-field assumption. Indeed, when the antenna size becomes large or the frequency increases, the interaction between the transmitting and receiving antennas can occur in the radiating near-field region. Here the wave approximation of the wavefront becomes inapplicable, and the actual spherical-shaped wavefronts must be considered instead. This unplumbed operating regime has been addressed [1, 2] as particularly favorable since it commences new and unexplored opportunities for future wireless systems, whose primary goal is to approach greater link-level spectrum efficiencies and unprecedented performance.

In light of this, a complete paradigm shift with respect to traditional, well-known approaches is required to tackle the open research challenges related to information transmission, channel modeling, radio space awareness acquisition and experimental validation [1], undoubtedly entailing the adoption of new strategies to deal with this innovative definition of the communication problem.

The remainder of this essay is organized as follows: Chapter 2 presents the general concept of smart radio environments (SREs) and intelligent surfaces, hence introducing the notion of communication modes and providing a general overview of the communication process between large intelligent surfaces (LISs). Chapter 3 describes the main features of OAM propagation and its potentialities, together with an outline of the state-of-the-art technologies and the latest discoveries related to OAM-based communications.
Then, the relationship between OAM and communication modes is illustrated, and the characteristics of OAM modes are discussed. In Chapter 4 various types of OAM-based communication schemes are presented. Moreover, focusing within the near field is introduced to improve system performance, thus counteracting the unavoidable phenomenon of beams' divergence. Chapter 5 accurately describes the software simulations that have been performed, thus proposing some numerical results to characterize the gap between OAM communications and optimum strategies in detail. Finally, a discussion concerning the main strengths and weaknesses of using OAM radio communication is provided, and Chapter 6 concludes the dissertation.

# Chapter 2

# Communication with Large Intelligent Surfaces

The first five generations of wireless networks have been designed based on the unmoving idea that the radio environment between two or multiple communicating devices is controlled by nature and cannot be modified in any manner; Inevitably, this led to the commonly shared belief that this behavior can only be compensated by developing sophisticated transmission and reception schemes.
Indeed, in current wireless networks, the radio channel is perceived as an adversary to the communication process, i.e., it mostly has a negative effect that needs to be counteracted by the transmitters and receivers through advanced modulation/encoding schemes, powerful transmission protocols, and robust demodulation/decoding methods at the receivers.
In contrast, the leading research direction that is establishing every day more within the academic world is that of transforming the wireless channel, i.e., the exogenous and uncontrollable element to which the telecommunication systems can only be adapted, into an intelligent, re-configurable space that plays an active role in transferring and processing information, i.e., in a so-called *smart radio environment* [3].
From all these considerations, the concept of *holographic communications* emerged [4], which can be referred to as the capability to utterly manipulate the EM field that is generated or received by antennas to exploit the entirety of the available channel's degrees of freedoms (DoFs) and hence increase the communication capacity of the wireless link, even in line-of-sight (LOS) channel conditions.

For this purpose, one of the most promising enabling technology that has been envisaged to accomplish this vision consists of exploiting the upcoming transmission technique named *intelligent surfaces* [5].
Specifically, LISs can be denoted as active, reconfigurable planar antennas whose sizes are much larger than the operating wavelength, that are able to control the amplitude and phase profiles of the EM waves with high flexibility and resolution [6, 7]. In addition to this, intelligent surfaces could also

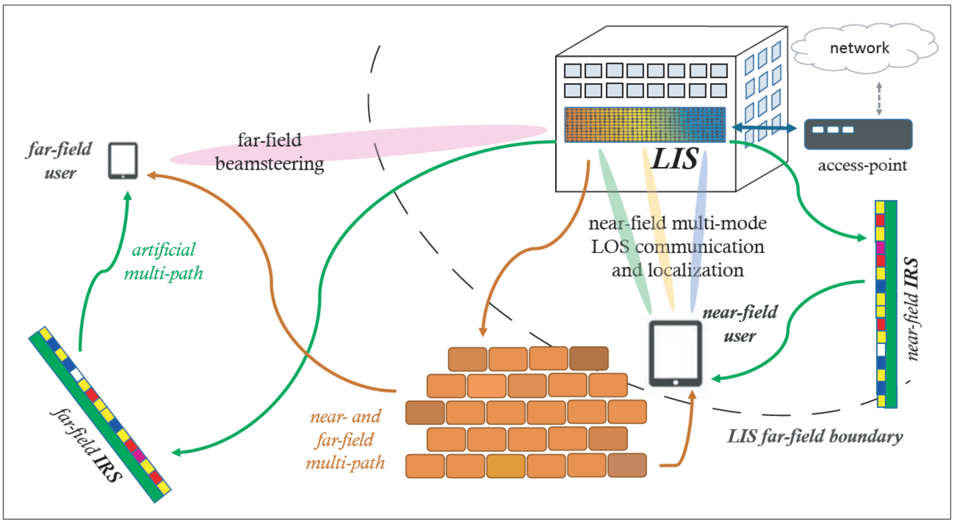

**Figure 2.1:** *Smart radio environment with a LIS antenna communicating with multiple users, both in the near and far fields, eventually assisted by intelligent reflective surfaces (IRSs) [4].*

be leveraged as passive, reflective devices, namely reconfigurable intelligent surfaces (RISs), to create artificial multipath transmissions between the end-users, hence establishing additional orthogonal communication channels [8]. Notably, metamaterials have been proposed [9–11] as a viable technology to create those kinds of smart devices, thus enabling the design of predefined EM waves' features in terms of shape, polarization, and steering.
For the sake of clarity, an insight of a SRE comprehending both RISs and LIS antennas is reported in Figure 2.1, illustrating how the adoption of these innovative wireless devices can enable a plethora of novel transmission modalities and use cases both in near and far-field conditions.

Noteworthily, the usage of large intelligent antennas in future wireless networks inherently renders the conventional system models obsolete, hence introducing the necessity of revisiting them in light of the fact that the system itself, i.e., the SRE, can be dynamically programmed. Indeed, in the presence of LISs/RISs, not only the channel input is an optimization variable, but the environment itself becomes an additional optimization element, and they clearly need to be optimized jointly [12].
The high versatility of this type of antenna and its intrinsic capability to achieve a multitude of novel functionalities at EM level also highlighted the vital importance of developing a tractable and insightful communication-theoretic framework for unveiling the achievable performance of LISs as a function of their many constituent parameters; Especially, because of the fact that their response to the impinging radio waves depends on several factors: the angle of reflection, the angle of refraction, the wave's polarization, the specific material the metasurface is composed of, and lots more.
In that regard, though abstracting from the specific implementation of those antennas, LISs can be generally modeled from the analytical viewpoint as

spatially-continuous apertures composed of an infinite number of infinitesimal antenna elements. In [7], the author investigated the fundamental limits of LIS-based communications and demonstrated how multiple communication modes, namely channel's DoFs, can be obtained in LOS and near-field regime by suitably designing the amplitude and phase profiles of the transmitting and receiving LISs.

Specifically, communication modes can be described as a set of parallel and orthogonal spatial channels, defined at EM level, thus enabling spatial multiplexing capabilities in the system. In the following section, the formal definition of communication modes is briefly illustrated. The reader can refer to [7, 13] for an exhaustive and more complete treatment.

## 2.1 Communication Modes

Abstracting in the first instance from the specific shape or antennas' configuration, let us generally consider a transmitting and a receiving LIS of area $S_\mathrm{T}$ and $S_\mathrm{R}$. We indicate with $\mathbf{s} \in S_\mathrm{T}$ and $\mathbf{r} \in S_\mathrm{R}$ the vectors pointing from the origin of the contemplated reference system towards a point on the transmitting LIS and the receiving one, respectively. At the transmitting LIS, a monochromatic source at frequency $f_0$, namely $\phi(\mathbf{s})$, is adopted, where $\mathbf{s}$ is the vector pointing from the origin to a point on the transmitting LIS. The source produces a wave function $\psi(\mathbf{r})$ which is collected by the receiving LIS, which is a solution of the inhomogeneous Helmholtz equation

$$\nabla^2\psi(\mathbf{r}) + \kappa^2\psi(\mathbf{r}) = -\phi(\mathbf{s})\,. \tag{2.1}$$

A solution of (2.1) in free-space conditions is given by

$$\psi(\mathbf{r}) = \int_{S_\mathrm{T}} G(\mathbf{r},\mathbf{s})\phi(\mathbf{s})\,\mathrm{d}\mathbf{s} \tag{2.2}$$

where $G(\mathbf{r}_1,\mathbf{r}_2)$ denotes the scalar Green function between points represented by vectors $\mathbf{r}_1$ and $\mathbf{r}_2$, which is

$$G\left(\mathbf{r}_1,\mathbf{r}_2\right) = \frac{\exp\left(-\jmath\kappa\,||\mathbf{r}_1-\mathbf{r}_2||\right)}{4\pi\,||\mathbf{r}_1-\mathbf{r}_2||} \tag{2.3}$$

with $\kappa = 2\pi/\lambda$ indicating the free-space wavenumber and $\lambda = c/f_0$ the wavelength, with $c$ standing for the speed of light. Notably, in (2.3) we are neglecting the reactive field components that typically vanish for link distances greater than a few wavelengths since our system is supposed to operate in the radiating near-field region.

Although the EM field is renowned for being a vectorial, complex quantity, in our analysis we consider it a complex-valued scalar quantity for simplicity (e.g., by considering a single polarization). Reasonably, the following results can be extended to the vectorial case without loss of generality or validity.

Communication modes can be described by the mean of specific orthonormal basis expansions of the transmitting function $\phi(\mathbf{s})$ and receiving function $\psi(\mathbf{r})$, indicated with $\{\phi_n(\mathbf{s})\}$ and $\{\psi_n(\mathbf{r})\}$, $n = 1, 2, ..., \infty$, respectively. If the basis sets are designed such that it exists a bijective relationship among the $n$-th transmitting basis function $\phi_n(\mathbf{s})$ and the $n$-th receiving basis function $\psi_n(\mathbf{r})$, the existence of multiple communication modes is assured. In view of this, it holds that each transmitting function $\phi_n(\mathbf{s})$ induces an effect $\xi_n \psi_n(\mathbf{r})$ on the receiving antenna space, where $\xi_n$ can be referred as the coupling coefficient. Large $\xi_n$ coefficients indicate well-coupled modes, i.e., pair of functions $(\phi_n(\mathbf{s}), \psi_n(\mathbf{r}))$, between transmitting and receiving LISs and hence practicable, parallel communication channels; small $\xi_n$ instead, denotes the prevalence of the transmitted wave's dispersion away from the receiver.
In relation to the particular system architecture, the factual interpretation of the previous quantities is that a generic current spatial distribution $J(\mathbf{s})$ impressed on the transmitting LIS and hence the resulting electric field $E(\mathbf{r})$ at the receiver side can be written, respectively, as

$$\begin{aligned} J(\mathbf{s}) &= \sum_n a_n \phi_n(\mathbf{s}) \\ E(\mathbf{r}) &= -\jmath\omega\mu_0 \sum_n b_n \psi_n(\mathbf{r}) \end{aligned} \tag{2.4}$$

where $\omega = 2\pi f_0$ is the angular frequency, $\mu_0$ is the free-space permeability, and $a_n$ and $b_n$ are the inner products of $J(\mathbf{s})$ and $\phi_n(\mathbf{s})$ and, correspondingly, of $-E(\mathbf{r})/\jmath\omega\mu_0$ and $\psi_n(\mathbf{r})$. In addition, it holds that $b_n = \xi_n a_n$. For simplicity, in the rest of this work we will refer to the functions $\psi_n(\mathbf{r})$ as $n$-th electric field component.

It should be noted that, in theory, infinite basis sets are possible in order to be complete; however, to obtain that corresponding to the highest number of communication modes with large coupling (optimal basis functions), the following coupled eigenfunction problem needs to be solved, i.e.,

$$\xi_n^2\, \phi_n(\mathbf{s}) = \int_{S_\mathrm{T}} K_\mathrm{T}(\mathbf{s}, \mathbf{s}')\, \phi_n(\mathbf{s}')\, \mathrm{d}\mathbf{s}' \tag{2.5}$$

$$\xi_n^2\, \psi_n(\mathbf{r}) = \int_{S_\mathrm{R}} K_\mathrm{R}(\mathbf{r}, \mathbf{r}')\, \psi_n(\mathbf{r}')\, \mathrm{d}\mathbf{r}' \tag{2.6}$$

where the kernels $K_\mathrm{T}(\mathbf{s}, \mathbf{s}')$ and $K_\mathrm{R}(\mathbf{r}, \mathbf{r}')$ are

$$K_\mathrm{T}(\mathbf{s}, \mathbf{s}') = \int_{S_\mathrm{R}} G^*(\mathbf{r}, \mathbf{s}) G(\mathbf{r}, \mathbf{s}')\, \mathrm{d}\mathbf{r} \tag{2.7}$$

$$K_\mathrm{R}(\mathbf{r}, \mathbf{r}') = \int_{S_\mathrm{T}} G(\mathbf{r}, \mathbf{s}) G^*(\mathbf{r}', \mathbf{s})\, \mathrm{d}\mathbf{s} \tag{2.8}$$

Finding these solutions is not straightforward and might require a burdensome number of numerical computations, especially when very large antenna

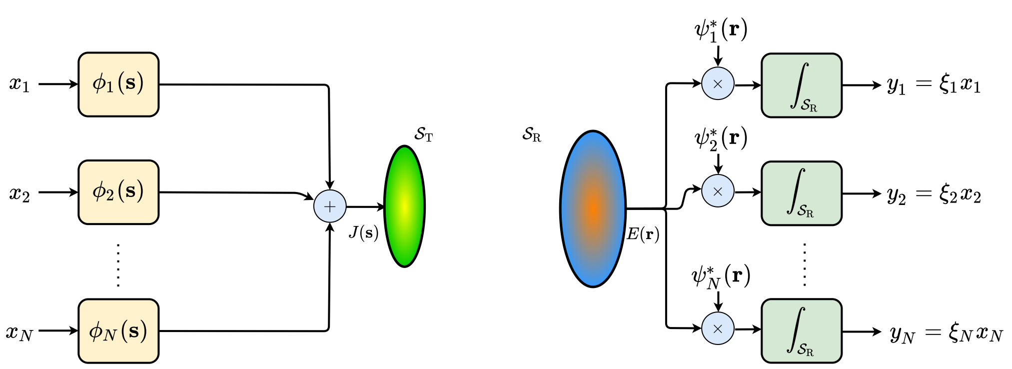

**Figure 2.2:** *Schematic representation of communication modes between a couple of LIS antennas.*

sizes are considered. Moreover, from the practical point of view, the exact knowledge of the system geometry with a tolerance smaller than a wavelength is required, which could not be practicable for real applications. Nevertheless, the optimal functions could be used as a benchmark to identify the performance gap between the optimal strategy and any other practical scheme exploiting sub-optimal basis function sets.
For this reason, sub-optimum strategies have been proposed, e.g., based on the approximation of the basis function sets with designated focusing/steering functions that depend on the specific operating conditions [14].

Overall, the communication problem can be seen as a wireless interconnection of continuous apertures with finite extension in space, capable of generating and detecting the most suitable EM waveforms to maximize the achievable channel capacity, even in LOS conditions. When only a finite number $N$ of basis functions are strongly coupled (i.e., with significant values of the corresponding $\xi_n$), the equivalent communication scheme which is obtained can be visualized as reported in Figure 2.2.
Remarkably, the adopted basis decomposition allows to define a system input-output representation in terms of $N$ parallel channels that is capacity-optimum, where $N$ identifies the available DoFs for the specific communication system. Indeed, by associating the $N$ input data streams $\{x_n\}$ to the transmitting basis set $\{\phi_n(\mathbf{s})\}$, $\mathbf{s} \in S_\mathrm{T}$, and neglecting the presence of noise, we are able to directly recover the transmitted data by performing the correlation of the received EM field with the corresponding basis functions $\{\psi_n(\mathbf{r})\}$, $\mathbf{r} \in S_\mathrm{R}$, thus obtaining $y_n = x_n \xi_n$, $n = 1, \ldots, N$.

## 2.2 Optimal communication modes with circular LISs

When limited antennas' sizes are considered, the optimal wave functions that describe the communication modes generated by circular apertures in paraxial conditions are the so-called circular prolate spheroidal functions (CPSFs) [15],

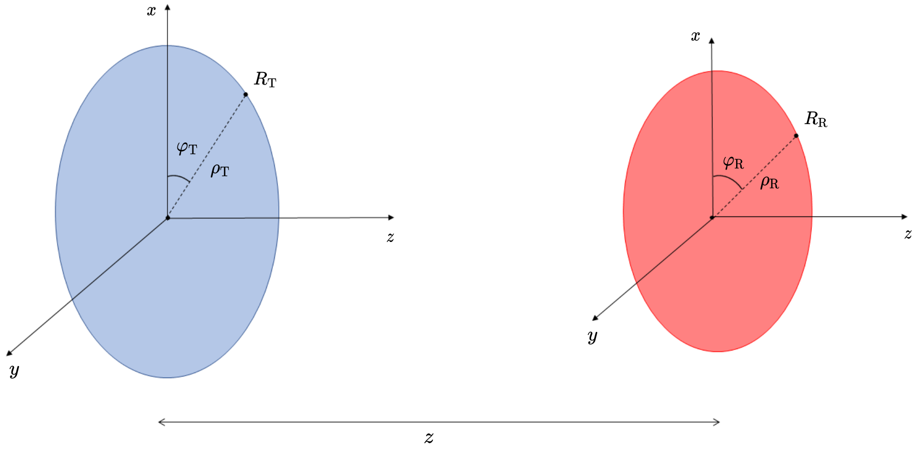

**Figure 2.3:** *Scenario with two LISs in paraxial conditions spaced of $z$.*

extending the classical linear prolate spheroidal wave functions (PSWFs), which are instead solutions under paraxial conditions for rectangular apertures [13].

With reference to Figure 2.3, consider two parallel, circular LISs in LOS. Polar coordinates $\rho_{\mathrm{T}}$ and $\varphi_{\mathrm{T}}$ describe a generic point on the transmitting LIS, while coordinates $\rho_{\mathrm{R}}$ and $\varphi_{\mathrm{R}}$ instead describe a generic point on the receiving LIS. The transmitting LIS is placed at $z = 0$, and the two LISs are spaced apart of $z$. Therefore, the transmitting LIS has a radius $R_{\mathrm{T}}$, while the receiving LIS has a radius $R_{\mathrm{R}}$. The distance between two generic points on the transmitting and receiving LISs is denoted as

$$r = |\mathbf{r} - \mathbf{s}| = \sqrt{\rho_{\mathrm{T}}^2 + \rho_{\mathrm{R}}^2 - 2\rho_{\mathrm{T}}\rho_{\mathrm{R}} \cos\left(\varphi_{\mathrm{R}} - \varphi_{\mathrm{T}}\right) + z^2} \tag{2.9}$$

. According to this geometry, the basis functions at the transmitting LIS are [15]

$$\phi_n(\rho_{\mathrm{T}}, \varphi_{\mathrm{T}}) = \frac{1}{\sqrt{2\pi R_{\mathrm{T}}\rho_{\mathrm{T}}}} f^c_{m,\ell}\left(\frac{\rho_{\mathrm{T}}}{R_{\mathrm{T}}}\right) e^{-\jmath\kappa\frac{\rho_{\mathrm{T}}^2}{2z}} e^{\jmath\ell\varphi_{\mathrm{T}}} \tag{2.10}$$

where $n = 1, \ldots, N$ are the indexes spanning the elements in the set $\mathcal{S} = \{m, \ell\}$ corresponding to well-coupled communications modes, $\{f^c_{m,\ell}\}$ are the real-valued CPSFs that solve the band-limited Hankel-transform eigenvalue problem

$$\gamma^c_{m,\ell} f^c_{m,\ell}(x) = \int_0^1 J_\ell\left(cxx'\right)\sqrt{cxx'} f^c_{m,\ell}\left(x'\right) \mathrm{d}x' \tag{2.11}$$

in which $\gamma^c_{m,\ell}$ are the eigenvalues, $c = \frac{\kappa R_{\mathrm{T}} R_{\mathrm{R}}}{z}$ is the bandwidth parameter, $x' = \frac{\rho_{\mathrm{T}}}{R_{\mathrm{T}}}$ and $x = \frac{\rho_{\mathrm{R}}}{R_{\mathrm{R}}}$. Correspondingly, at the receiver side we have the basis functions [15]

$$\psi_n(\rho_{\mathrm{R}}, \varphi_{\mathrm{R}}) = \frac{1}{\sqrt{2\pi R_{\mathrm{R}}\rho_{\mathrm{R}}}} \frac{e^{\jmath\kappa z}}{\jmath^\ell} f^c_{m,\ell}\left(\frac{\rho_{\mathrm{R}}}{R_{\mathrm{R}}}\right) e^{\jmath\kappa\frac{\rho_{\mathrm{R}}^2}{2z}} e^{\jmath\ell\varphi_{\mathrm{R}}} . \tag{2.12}$$

According to [15], the coupling coefficient for the communication modes are

$$\xi_n = \gamma^c_{m,\ell}\sqrt{\frac{R_{\mathrm{T}} R_{\mathrm{R}}}{4\kappa z}} . \tag{2.13}$$

Due to the properties of the eigenvalues $\gamma^{c}_{m,\ell}$ related to CPSFs, the number of communication modes (i.e,. well-coupled modes) is given by [15]

$$N = \left(\frac{\pi R_{\mathrm{T}} R_{\mathrm{R}}}{\lambda z}\right)^2 = \frac{S_{\mathrm{T}} S_{\mathrm{R}}}{\lambda^2 z^2} \tag{2.14}$$

where $S_{\mathrm{T}} = \pi R_{\mathrm{T}}^2$ and $S_{\mathrm{R}} = \pi R_{\mathrm{R}}^2$ are the areas of the LISs. Incidentally, Equation (2.14) has the same form of classical results related to rectangular surfaces [13].

Notably, both the transmitting and receiving basis functions $\phi_n(\rho_{\mathrm{T}}, \varphi_{\mathrm{T}})$ and $\psi_n(\rho_{\mathrm{R}}, \varphi_{\mathrm{R}})$ are separable in $\rho$ and $\varphi$, that is, they can be written respectively as

$$\begin{aligned} \phi_n(\rho_{\mathrm{T}}, \varphi_{\mathrm{T}}) &= \phi_n^{\rho}(\rho_{\mathrm{T}})\, \phi_n^{\varphi}(\varphi_{\mathrm{T}}) \\ \psi_n(\rho_{\mathrm{R}}, \varphi_{\mathrm{R}}) &= \psi_n^{\rho}(\rho_{\mathrm{R}})\, \psi_n^{\varphi}(\varphi_{\mathrm{R}})\,. \end{aligned} \tag{2.15}$$

# Chapter 3

# Orbital Angular Momentum

From the physical viewpoint, electrons are elementary quantum particles that exhibit the wave-particle duality characterizing all the existing quantistic entities. Generally, the particles' properties can be easily described employing classical electrodynamics, like the well-known Lorentz's force and Coulomb's law, while the wave features of electrons are precisely specified by quantum mechanics and Schrödinger's equation.

An accurate and complete description of an electromechanical system needs to consider both its translational dynamics and its rotational one. In particular, the former is physically described by the varying linear momentum, i.e., forces. In the case of wireless communications, radio transmissions are based on the transfer of the linear momentum density, hence what is usually referred in the literature as the Poynting vector.
Rotational dynamics instead is physically described by the variation of angular momentum, thus by the bodies' revolution according to Newtonian mechanics and the second Euler's law [16].

## 3.1 General Definition

From the EM point of view, angular momentum is a vectorial characteristic that quantitatively defines the intrinsic rotation of the EM field.
While propagating in the axial direction indeed, a photons' fashion can simultaneously rotate around its axis. In addition, there are two different modalities of rotation, and each of them is associated with a specific component of the total angular momentum.
Particularly, the total angular momentum can be computed as the sum of the spin angular momentum (SAM) and the orbital angular momentum (OAM). The SAM is related to the dynamic rotation of the electromagnetic field around its direction of propagation, and it is intrinsically related to the wave's polarization [17]. OAM instead concerns the spatial distribution of the electromagnetic field and its rotation around the main beam axis [16].
Notably, the main difference between these two wave's components relies upon

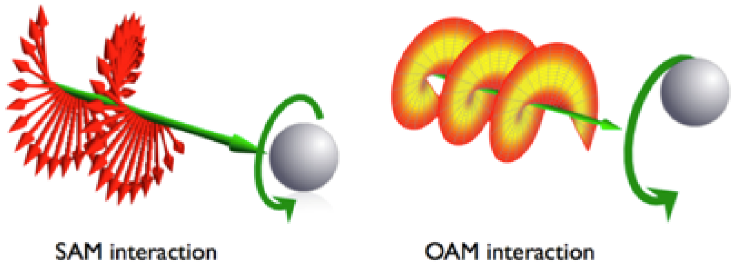

**Figure 3.1:** *The illustrative distinction between the SAM (left) and OAM components (right) of the EM angular momentum.*

the fact that OAM beams, i.e., with zero SAM, have *rotating wavefronts*, while polarized beams, namely with zero OAM and only non-null SAM component, have *rotating electric field vector*, as depicted in Figure 3.1.

Specifically, the main peculiarity of EM waves with non-null OAM relies on the insurgence of wavefronts that are not parallel planes propagating in the axis direction, as in the classical far-field assumption, rather than continuous, helical-shaped wavefronts that are torqued around the propagation direction and with a phase singularity in their center. In particular, this last element is a point of destructive interference in which the EM field intensity is zero and its phase distribution is indeterminate.
Indeed, by sectioning those vortices along the vertical direction, i.e., the direction that is perpendicular to the wave's propagation plane, this characteristic might be visualized as a light intensity ring with a hole in its middle as shown in Figure 3.2.
For this reason, OAM is frequently described as a vortex or with the notion of helical/twisted/screwed wavefront.

The aforementioned physical quantities can be expressed as [18]

$$\boldsymbol{J} = \boldsymbol{S} + \boldsymbol{L} \tag{3.1}$$

i.e., the total angular momentum $\boldsymbol{J}$ of the EM field associated with a volume $V$ can be decomposed as the sum of the SAM component $\boldsymbol{S}$ and the OAM component $\boldsymbol{L}$. These two can be computed as [19]

$$\boldsymbol{S} = \epsilon_0 \int_V \mathfrak{Re}\{\boldsymbol{E}^* \times \boldsymbol{A}\}\,\mathrm{d}V \tag{3.2}$$

$$\boldsymbol{L} = \epsilon_0 \int_V \mathfrak{Re}\{\jmath \boldsymbol{E}^* (\tilde{\boldsymbol{L}} \cdot \boldsymbol{A})\}\,\mathrm{d}V \tag{3.3}$$

where $\epsilon_0$ is the dielectric constant in vacuum, $\boldsymbol{r}$ is the radius vector of a point in the electric field, $\tilde{\boldsymbol{L}} = -\jmath(\boldsymbol{r} \times \nabla)$ is the OAM operator, $\boldsymbol{E}$ is the electric field, $\boldsymbol{A}$ is the vector potential and $\jmath$ the imaginary unit, while $\mathfrak{Re}\{\cdot\}$ and $(\cdot)^*$ represent the real part operation and the conjugate operator respectively.

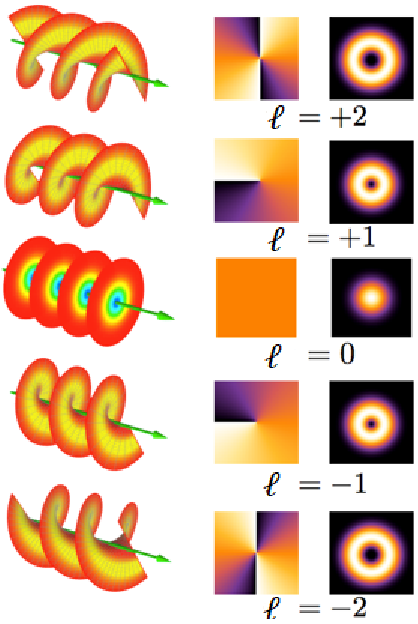

**Figure 3.2:** *Plot of the propagating twisted wavefronts (left) and the phase and intensity distribution, respectively, of the OAM beams (right) for different* $\ell$ *values.*

Remarkably, a complete vectorial description of the EM field is required to characterize its specificity in terms of OAM. However, albeit considering the scalar approximation as in Chapter 2, the specific helical structure of the wavefronts characterizing OAM is generally described in the wave equation by an exponential phase term, that is $e^{\jmath\ell\varphi}$, where $\ell \in \mathbb{Z}$ is the so-called *topological charge* and $\varphi$ is the transverse azimuthal angle, defined as the angular position on a plane perpendicular to the propagation direction.
In [17], it has been demonstrated that this characteristic constitutes a sufficient condition to have OAM-carrying waves when in the presence of a propagation regime that is mostly paraxial.
As a matter of fact, each vortex is hence characterized by an integer number $\ell$, whose module identifies the number of twists that a wavefront performs within a distance equal to the wavelength, while its sign determines the chirality, that is, the direction of the twist. In fact, when $|\ell| > 0$, the wavefront characterizing a specific topological charge has $|\ell|$ helices intertwined. Each of these states associated with a specific topological charge $\ell$ takes the name of OAM mode.

The interesting property of OAM modes is their inherent orthogonality. In fact, it holds

$$\int_0^{2\pi} e^{\jmath\ell_j\varphi}(e^{\jmath\ell_k\varphi})^* \, \mathrm{d}\varphi = \begin{cases} 0 & j \neq k \\ 2\pi & j = k \end{cases} \tag{3.4}$$

thus, in principle, beams exhibiting this characteristic could carry different data streams, hence leading to the introduction of spatial multiplexing capabilities in the communication system under study.

Many types of beams, i.e., OAM modes, carrying angular momentum have been investigated throughout the years to impress the EM waves the desired vorticose phase profile, among which Laguerre-Gaussian (LG) beams are probably the most widely known. Precisely, LG beams are paraxial solutions of the wave equation in homogeneous media.
In cylindrical coordinates, a generic EM wave propagating in free space along the $z$-direction can be expressed as [20]

$$E(\rho, \varphi, z) = u(\rho, \varphi, z) e^{-\jmath \kappa z} \tag{3.5}$$

where $u(\rho, \varphi, z)$ is the complex amplitude distribution of the EM field. Specifically, for an LG beam propagating along the $z$-axis, it holds [17]

$$\begin{aligned} u(\rho, \varphi, z) = & \sqrt{\frac{2p!}{\pi w^2(z)(p+|\ell|)!}} \left[\frac{\rho\sqrt{2}}{w(z)}\right]^{|\ell|} L_p^{|\ell|}\left(\frac{2\rho^2}{w^2(z)}\right) \exp\left[\frac{-\rho^2}{w^2(z)}\right] \\ & \times \exp\left[\frac{\jmath \kappa \rho^2 z}{2\left(z^2+z_R^2\right)}\right] \exp(\jmath \ell \varphi) \exp\left[-\jmath(2p+|\ell|+1)\tan^{-1}\left(\frac{z}{z_R}\right)\right] \end{aligned} \tag{3.6}$$

where $w(z) = w_0\left[\left(z^2+z_R^2\right)/z_R^2\right]^{1/2}$ is the radius of the beam, $w_0$ is the waist radius, $z_R = \frac{\pi w_0^2}{\lambda}$ is the Rayleigh range, i.e. the distance along the propagation direction from the beam waist to the point where the area of the cross section is doubled [21], $L_p^{|\ell|}(x)$ is the associated Laguerre polynomial and $(2p+|\ell|+1)\tan^{-1}(z/z_R)$ is the Gouy phase.

Another well-known category of OAM waves are the Bessel beams, which can be described as

$$u(\rho, \varphi, z) = J_\ell\left(\kappa_\rho \rho\right) e^{\jmath \kappa_z z} e^{\jmath \ell \varphi} \tag{3.7}$$

where $J_\ell(\cdot)$ is the $\ell$-order Bessel function of the first kind and $\kappa_\rho$ and $\kappa_z$ are the radial and axial wavenumbers, respectively [18].

The two kinds of EM waves mentioned above are just a few of the plethora of existing waves able to carry angular momentum: Gaussian beams, Airy beams, and many others were subjects of research [22,23], representing possible solutions to the problem of determining the best field distribution for OAM propagation. Apparently, the common element between these kinds of beams is that all of them are reasonably able to transport orbital angular momentum, and this characteristic is always described from the mathematical viewpoint through the exponential term $e^{\jmath \ell \varphi}$.

## 3.2 State of The Art

Noticeably, many relevant applications exploiting OAM properties have been envisaged in the latest years. For instance, a novel type of space-division multiplexing technique based on modes' orthogonality has been theorized, namely OAM mode-division multiplexing (OAM-MD) [24], which could be used jointly

with the most varied modulation formats as well as the existing multiplexing techniques based on time, frequency and polarization (TDM, FDM, PDM) to increase system capacity significantly.
Moreover, multi-level coding techniques (OAM-SK) able to code the information through the specific value of the topological charge $\ell$ have been suggested, together with the possibility of managing the increasing users' density through an OAM-based multiple access scheme (OAM-MDMA) [25].
In addition to this, an extensive number of possible technologies and deployments were proposed, dealing with many wireless communications sectors. Mode hopping techniques [26], OAM-MIMO systems [27, 28], OFDM-OAM modulations [29], radar targets imaging [30], indoor or near-field communications [31] are very few of the use cases that have been studied throughout the last decade and, in particular areas of research, some solutions have been already deployed; In particular in the optical domain for biological cells and particles manipulation or radioastronomy for extra-solar planets coronography. However, a very small number of works to date effectively investigate the potentialities of exploiting OAM with intelligent surfaces, especially when the communication occurs in the near-field propagation regime.

The major adversities and drawbacks in developing these visionary ideas and their relative applications lie in the several problems that OAM propagation displays and their interference with the correct data reception at the receiver side. The unwanted effects that need to be counteracted are the following:

- *Beam divergence*: it has been proven that OAM beams diverge from their central axis as $\sqrt{\ell}$ [32]. What is more, higher-orders OAM modes diverge even more rapidly than their lower-orders counterparts. An insight of this undesired physical phenomenon is reported in Figure 3.3a.

- *Misalignment between transmitter and receiver*: lateral displacement and receiver angular errors are the most common dislocations that can occur in a non-paraxial regime, as depicted in Figure 3.3b.

- *Atmospheric turbulence*: propagation disturbances may arise due to refractive index variations related to temperature and pressure inhomogeneities that are present in the radio space. This effect is extremely detrimental since it can utterly destroy the helical wavefront and hence destroy the phase information content [33], as shown in Figure 3.4.

- *Multipath*: this effect can be caused both by reflections and beam spreading. It has been shown that OAM channels with high $\ell$ undergo larger intra- and inter-channel interference due to beams divergence during the propagation.

All the issues mentioned above unavoidably lead to significant power loss and crosstalk interference at the receiver side and, at its extreme, can also determine the complete destruction of the wavefronts, hence loss of information.

For this reason, the future of OAM communications is forecast by many to be mainly related to LOS scenarios and near-field communications [34].

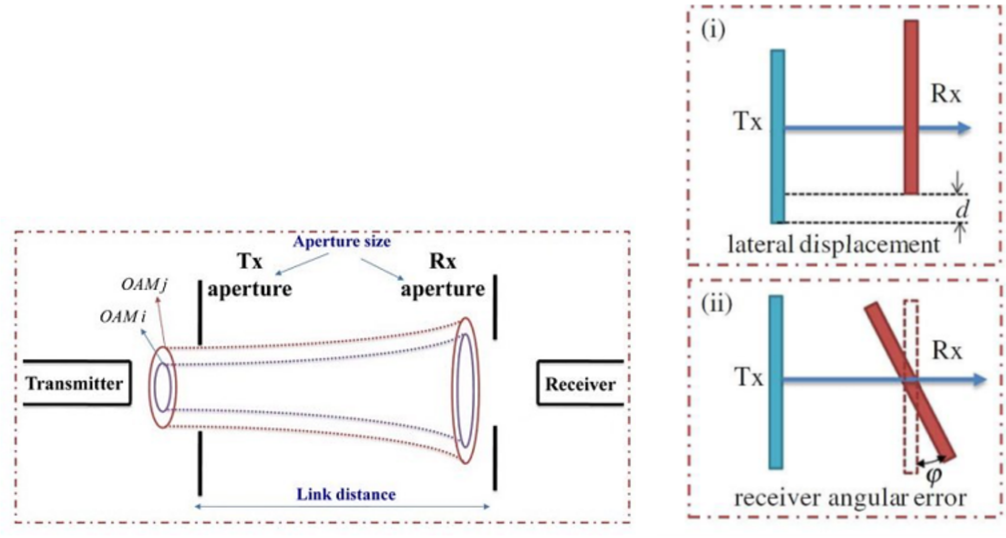

**(a)** **(b)**

**Figure 3.3:** *A graphic representation of the beam divergence phenomenon* (a) *and the possible misalignment errors* (b) *that can occur at the receiver side [32].*

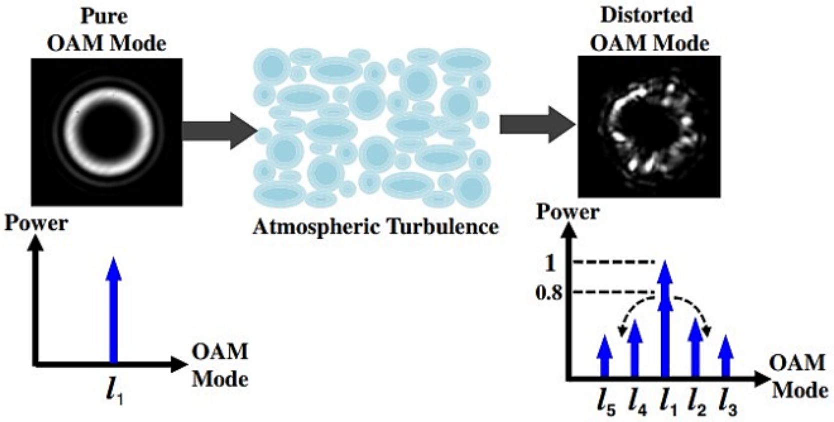

**Figure 3.4:** *Illustration of the effects of atmospheric turbulence on OAM vortexes propagation, leading to distortion and inter-modal interference [33].*

## 3.3 Experimental Validations and Contributions

Not only theoretical research and simulations have been carried out by the scientific community worldwide, but also a great number of experiments were performed to validate the effective capability to transmit information through light twists.

First and foremost, it is important to mention the renowned Venice experiment [35] in which two different tones were transmitted simultaneously on the same 2.4 GHz frequency band in LOS condition from the lighthouse of San Giorgio island to the balcony of Venice's Palazzo Ducale, separated by a total length of 442 meters (See Figure 3.5). The two distinct radio signals were broadcast on different OAM channels, $\ell = 0$ and $\ell = +1$, respectively, and the receiver was then able to successfully detect both channels through an interferometric phase discrimination method that put in evidence the phase fingerprints due to the twisting of electromagnetic waves. For greater clarity, a depiction of the specific radio detector that has been used is reported in Figure 3.6.

This result held a broad appeal globally since, originally, it seemed like the first experimental proof that OAM modes can propagate coherently at radio frequencies and be detected correctly in the far-field. Nonetheless, this gave rise to a vivid debate [36–38], that ended with the counterpart's demonstration that the OAM multiplexing scheme presented in [35] can be used for large distances between the transmitter and the receiver (i.e., $z$) only if the receiving antennas spacing $d$ is increased proportionally to $z$. Indeed, if the distance $d$ between the receiving antennas is kept constant, it was shown that an additional power decay $z^{-2(|\ell|+1)}$ emerges in the case of LG beams, preventing any capacity gain in the far-field. If instead, $d$ is increased proportionally to the transmitting-receiving antennas distance $z$, then the same result can be obtained with an alternative, well-known antennas setup, e.g., MIMO. In that way, it was proved that OAM modes are not necessarily required for such a result.

**(a)** **(b)**

**Figure 3.5:** (a) *The satellite view of Venice's canal where the first OAM broadcast transmission took place.* (b) *Venice's Palazzo Ducale displaying the writing "signal received", after the successful reception of the OAM multiplexed signal.*

Another interesting proof was delivered by the same Italian research group that carried on further experiments in Padua [39]. This time the transmitted

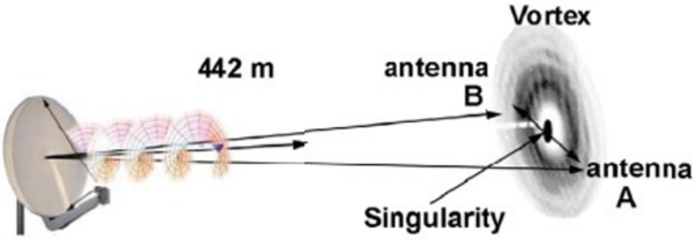

**Figure 3.6:** *Illustration of the phase interferometer utilized for Venice's experiment, composed of two connected receiving antennas connected through a* 180° *phase-shift cable.*

OAM channels were three, $\ell = 0$, $\ell = -1$ and $\ell = +1$ precisely, at a frequency of 17.128 GHz and the tests were performed in LOS condition for several link distances in the order of a hundred meters. Also in this trial, the results were significant, displaying relevant inter-modal isolation without the need for digital post-processing.

The aforementioned experiments were just a few of the several practical examinations that have been executed by researchers, and, intuitively, many open issues and problems are still to be addressed; particularly, in light of the fact that OAM-based communication performance was shown to be strongly affected by the kind of antenna that is used, the overall systems architecture, the operating frequency, and many other elements.
In particular, a plethora of radio OAM generation methods have been identified, and each of them has its specific advantages and drawbacks concerning cost, complexity, market readiness, and working frequency.
Spiral phase plate (SPP) antennas, spiral reflectors, uniform circular antenna arrays (UCAAs), and metasurfaces were all subjects of research by many academics, and, in the end, every OAM signal generation technique was identified as optimal for a specific operating frequency. For instance, previous works, e.g., [18] to mention one, reported that spiral reflectors and UCAAs work best at RF frequencies and are more suitable for long-range transmissions, while SPPs and metasurfaces are better for the mmWaves band.

Moreover, the relationship of this new OAM-based transmission technique with the most advanced wireless communication systems and methodologies has been investigated, especially in relation to MIMO systems and beamforming [27,40–42]. Unfortunately, few improvements and many unsolved questions have been highlighted, making it still an open and intricate debate.

## 3.4 Interpretation

From the analytical point of view, an important distinction has to be made with respect to the mathematical formulation and the results derived in the previous chapter.

The main difference concerning the definition of the OAM modes as in (3.6)-(3.7) with respect to the optimal basis sets (2.10)-(2.12) is that neither concepts nor references related to the specific transmitting/receiving antennas are given. Differently, communication modes, as identified by the couples of functions $(\phi_n(\mathbf{s}), \psi_n(\mathbf{r}))$, are strictly related to the geometry of the transmitting and receiving antennas.

The explanation of their dissimilarity resides exactly in the different definitions of modes. While LG beams are solutions of the wave equation evaluated in the absence of boundaries, i.e., with the source's transverse dimensions at infinity, communication modes in Chapter 2 are instead obtained by considering finite antenna sizes. As a consequence, LG modes can be considered as approximations of the actual propagating modes when the transmit aperture is large enough to generate the beams and the receive aperture is extended enough to capture them [15].

In theory, many categories of existing beams are suitable for describing paraxial wave propagation carrying OAM and these solutions could suggest that an unlimited number of channels would be available. However, when boundaries corresponding to finite transmit/receive antennas are considered, a limited number $N$ of well-coupled communication modes is obtained, and LG beams do not constitute proper solutions of (2.1) [43].

Given the basis functions' separability as in (2.15), the helical phase-front characterizing OAM-based propagation can be obtained by impressing a phase rotation through the azimuthal component of the transmitting basis function $\phi_n^{\varphi}(\varphi_{\mathrm{T}}) = e^{\jmath \ell \varphi_{\mathrm{T}}}$. Then, according to (2.2), we obtain a wave given by

$$\psi(\rho_{\mathrm{R}}, \varphi_{\mathrm{R}}, z) = \int_0^{R_{\mathrm{T}}} \rho_{\mathrm{T}} \phi_n^{\rho}(\rho_{\mathrm{T}}) \int_0^{2\pi} e^{\jmath \ell \varphi_{\mathrm{T}}} f(\rho_{\mathrm{T}}, \rho_{\mathrm{R}}, \cos(\varphi_{\mathrm{R}} - \varphi_{\mathrm{T}}))\, \mathrm{d}\varphi_{\mathrm{T}}\, \mathrm{d}\rho_{\mathrm{T}} \tag{3.8}$$

where

$$f(\rho_{\mathrm{T}}, \rho_{\mathrm{R}}, \cos(\varphi_{\mathrm{R}} - \varphi_{\mathrm{T}})) = \frac{e^{-\jmath \kappa r}}{4\pi r} \tag{3.9}$$

having defined $r$ in (2.9). Thus, with a change of variable $\alpha = \varphi_{\mathrm{T}} - \varphi_{\mathrm{R}}$, it is obtained

$$\psi(\rho_{\mathrm{R}}, \varphi_{\mathrm{R}}, z) = e^{\jmath \ell \varphi_{\mathrm{R}}} g_n(\rho_{\mathrm{R}}, z) \tag{3.10}$$

which is again separable in $\rho_{\mathrm{R}}$ and $\varphi_{\mathrm{R}}$, and

$$g_n(\rho_{\mathrm{R}}, z) = \int_0^{R_{\mathrm{T}}} \rho_{\mathrm{T}} \phi_n^{\rho}(\rho_{\mathrm{T}}) \int_0^{2\pi} e^{\jmath \ell \alpha} f(\rho_{\mathrm{R}}, \rho_{\mathrm{T}}, \cos(\alpha))\, \mathrm{d}\rho_{\mathrm{T}}\, \mathrm{d}\alpha\,. \tag{3.11}$$

It can be noticed from Equation (3.10) that the exponential term $e^{\jmath \ell \varphi_{\mathrm{R}}}$ identifying OAM is also present in the received EM field expression. This shows that OAM wavefronts propagate in free-space with no changes and irrespectively of the selected transmitting amplitude profile, thus demonstrating how orthogonality among OAM-based modes is preserved at the receiver. However, the phase factor at the transmitter side leading to OAM unavoidably affects the shape of the beam along the radial coordinate $\rho_\mathrm{R}$, in particular causing the well-known beam divergence [32], as it will be characterized in the followings.

# Chapter 4

# OAM-based Communication using LISs

Ideally, it is evident that the adoption of CPSFs as basis functions according to (2.10) and (2.12) leads to the highest number of communication modes. Unfortunately, such an approach results quite complex to be implemented, even in the paraxial scenario, for several reasons:

- The transmitting and receiving LISs should know exactly their mutual distance, rotation, and size in order to shape the amplitude and phase profiles along the transverse radial coordinates $\rho_\mathrm{T}$ and $\rho_\mathrm{R}$;
- A complex amplitude/phase profile must be drawn at the transmitter side according to (2.10). Similarly, the received EM field must be properly weighted with a complex amplitude/phase profile according to (2.12). These operations require high hardware flexibility at both the LISs, which could not be affordable, especially at high frequencies.

To simplify both the transmitting and receiving LISs architectures and exploit, at the same time, the multiplexing capabilities offered by the OAM helical wavefronts, a viable solution is to resort to functions of more straightforward realization.
In particular, recalling the OAM conservation property demonstrated in Equation (3.10), we assume here to use the following orthonormal basis functions at the transmitter side

$$\phi_n(\rho_\mathrm{T}, \varphi_\mathrm{T}) = \frac{1}{\sqrt{2\pi R_\mathrm{T}}} e^{\jmath \ell_n \varphi_\mathrm{T}} \tag{4.1}$$

with

$$\ell_n = \begin{cases} -\frac{n-1}{2} & \mathrm{mod}\ (n,2) = 1 \\ \frac{n}{2} & \mathrm{mod}\ (n,2) = 0 \end{cases} \tag{4.2}$$

where $n = 1, \ldots, N$ and, consequently, $\ell_n = 0, +1, -1, +2, -2, \ldots, (N-1)/2$, assuming $N$ odd. Thus, we consider $\phi_n(\rho_\mathrm{T}, \varphi_\mathrm{T}) = \phi_n^\rho(\rho_\mathrm{T})\phi_n^\varphi(\varphi_\mathrm{T})$ where

$$\phi_n^\rho(\rho_\mathrm{T}) = \frac{1}{\sqrt{R_\mathrm{T}}}\Pi_{R_\mathrm{T}}(\rho_\mathrm{T}) \tag{4.3}$$

$$\phi_n^\varphi(\varphi_\mathrm{T}) = \frac{1}{\sqrt{2\pi}}e^{\jmath \ell_n \varphi_\mathrm{T}} \tag{4.4}$$

with

$$\Pi_a(\xi) = \begin{cases} 1 & \xi \in (0, a) \\ 0 & \text{otherwise} \end{cases} \tag{4.5}$$

being the rectangular function, which in our specific case identifies a circle of radius $a$ when used in Equation (4.3).
These bases can be viewed as the extension to a circular surface of the typical phase tapering profiles required to generate OAM waves with uniform circular arrays (UCAs). In fact, a well-known technique for obtaining the helical wavefront consists of feeding a circular array of $N_\mathrm{TX}$ elements equispaced over a ring, with a successive phase delay $\Delta = 2\ell\pi/N_\mathrm{TX}$ such that, after a full turn, the phase is incremented of a multiple integer $\ell$ of $2\pi$ (i.e., phase varies linearly with the azimuthal angle) [44].
Functions (4.1) are orthonormal as well and could be used to realize spatial multiplexing by requiring phase-tapering only in order to generate the EM field, thus drastically reducing the LIS complexity. Clearly, these functions do not form a complete basis set, unlike the optimum solutions, and hence a performance degradation in terms of DoFs is expected.
Notice that $n = 1$ (i.e., $\ell_n = 0$) corresponds to a uniform feed over the transmitting LIS, then the obtained beam is that typical of a uniform circular aperture. The other modes are always degenerate, and hence the same coupling is obtained for two consecutive modes (e.g., for $n = 2$ and $n = 3$, corresponding to the topological charges with the same absolute values and opposite chirality).

When the basis function $\phi_n(\rho_\mathrm{T}, \varphi_\mathrm{T})$ is adopted at the transmitting antenna according to (4.1), the field at the generic distance $z$ is given by (2.2) and has the same form of (3.10), that is

$$\psi^{(n)}(\rho_\mathrm{R}, \varphi_\mathrm{R}, z) = \frac{1}{\sqrt{2\pi R_\mathrm{T}}} \int_0^{R_\mathrm{T}} \int_0^{2\pi} e^{\jmath \ell_n \varphi_T} \frac{e^{-\jmath \kappa r}}{4\pi r} \rho_\mathrm{T} \, \mathrm{d}\varphi_\mathrm{T} \, \mathrm{d}\rho_\mathrm{T} \tag{4.6}$$

Here we used the notation $\psi^{(n)}(\rho_\mathrm{R}, \varphi_\mathrm{R}, z)$ to indicate the $n$-th component of the received EM field when the $n$-th basis function $\phi_n(\rho_\mathrm{T}, \varphi_\mathrm{T})$ in (4.1) was used.
In particular, considering waves propagation within the Fresnel zone, where multiple communication modes can be realized [14], we can approximate $r$ in the numerator of (4.6) with

$$r \approx z + \frac{\rho_\mathrm{T}^2}{2z} + \frac{\rho_\mathrm{R}^2}{2z} - \frac{\rho_\mathrm{T}\rho_\mathrm{R}\cos(\varphi_\mathrm{R} - \varphi_\mathrm{T})}{z} \tag{4.7}$$

and assume $r \approx z$ in the denominator of (4.6). This classical Fresnel approximation allows writing the received EM field as

$$\begin{aligned}\psi^{(n)}(\rho_\mathrm{R}, \varphi_\mathrm{R}, z) &= \frac{1}{4\pi z\sqrt{2\pi R_\mathrm{T}}} e^{-\jmath\kappa\frac{\rho_\mathrm{R}^2}{2z}} e^{-\jmath\kappa z} \\ &\times \int_0^{R_\mathrm{T}} \int_0^{2\pi} e^{\jmath\ell_n\varphi_\mathrm{T}} e^{-\jmath\kappa\frac{\rho_\mathrm{T}^2}{2z}} e^{\jmath\kappa\frac{\rho_\mathrm{R}\rho_\mathrm{T}\cos(\varphi_\mathrm{R}-\varphi_\mathrm{T})}{z}} \rho_\mathrm{T}\,\mathrm{d}\varphi_\mathrm{T}\,\mathrm{d}\rho_\mathrm{T} \\ &= \frac{(-1)^{\ell_n}}{2z\sqrt{2\pi R_\mathrm{T}}} e^{-\jmath\kappa\frac{\rho_\mathrm{R}^2}{2z}} e^{-\jmath\kappa z} e^{\jmath\ell_n\varphi_\mathrm{R}} \int_0^{R_\mathrm{T}} \rho_\mathrm{T} e^{-\jmath\kappa\frac{\rho_\mathrm{T}^2}{2z}} J_{\ell_n}\left(\frac{\kappa\rho_\mathrm{R}\rho_\mathrm{T}}{z}\right) \mathrm{d}\rho_\mathrm{T}\,.\end{aligned} \tag{4.8}$$

When $N$ data streams are transmitted simultaneously, in order to carry the data symbols $\mathbf{x} = \{x_1, \dots, x_N\}$ according to the basis functions $\phi_n(\rho_\mathrm{R}, \varphi_\mathrm{R})$ in (4.1) for exploiting spatial multiplexing, the overall received EM field at a distance $z$ from the transmitting antenna is

$$\psi(\rho_\mathrm{R}, \varphi_\mathrm{R}, z) = \sum_{n=1}^{N} x_n \psi^{(n)}(\rho_\mathrm{R}, \varphi_\mathrm{R}, z)\,. \tag{4.9}$$

Subsequently, the EM field $\psi(\rho_\mathrm{R}, \varphi_\mathrm{R}, z)$ is processed by the receiving LIS in order to extract the information data $\mathbf{x}$, as discussed in the following sections.

## 4.1 Focused OAM

When considering the OAM-based EM field according to what has been discussed so far, it can be noticed from the analytical expression in (4.8) that the higher-order beams display maxima for increasingly larger values of $\rho_\mathrm{R}$, following the typical behavior of Bessel's functions. Indeed, it is well-known that OAM beams diverge increasingly with the growth of the topological charge [32]. Therefore, a large receiving LIS is required to collect most of the beam and obtain a significant coupling intensity, hence a correct data reception. This discussion highlights an intrinsic, critical issue in exploiting OAM with UCAs at the receiver side: in fact, a fixed-radius UCA would be able to collect significant energy from the OAM beam only if its radius is collimated with the corresponding beam divergence at a given distance. However, since every topological charge exhibits a different divergence effect, the receiving circular array will be suitable for correctly detecting (i.e., with good coupling) only a certain predefined mode, being sub-optimal for the others. In this sense, the use of a large receiving LIS enables much more flexibility and larger coupling intensities for a larger number of modes.

Moreover, the beam widening effect is emphasized when operating within the near-field since the diffraction pattern of an aperture is intrinsically larger than the one obtained in the far-field, being the result of a convolution with a quadratic-phase term, as highlighted in (4.8).

A renowned technique for limiting the angular spread of a beam in the near field is focusing [45]. This process consists in adjusting the phase of a radiating source so that it compensates for the propagation delay towards a specific point (the focal point), where all the field contributions add coherently, thus enhancing the EM field intensity in a limited-area region (i.e., beam with finite depth).
To reach such a result using the functions considered in (4.1), a modification of the transmitting phase profile $\phi_n(\rho_{\mathrm{T}}, \varphi_{\mathrm{T}})$ along the transverse radial coordinate $\rho_{\mathrm{T}}$ can be realized, making the phase along this coordinate converging at the targeted focal point. Considering the paraxial geometry, with the focal point corresponding to the center of the receiving LIS at a distance $z$, this corresponds to assume

$$\phi_n^{\rho}(\rho_{\mathrm{T}}) = \frac{1}{\sqrt{R_{\mathrm{T}}}}\, e^{\jmath\kappa r}\big|_{\rho_{\mathrm{R}}=0} \approx \frac{1}{\sqrt{R_{\mathrm{T}}}} e^{\jmath\kappa z\left(1+\frac{\rho_{\mathrm{T}}^2}{2z^2}\right)} \tag{4.10}$$

where the right-hand approximation comes from the Fresnel approximation in (4.7). From a practical viewpoint, focusing can be implemented according to $\phi_n^{\rho}(\rho_{\mathrm{T}}) = \exp\left(\jmath\kappa\rho_{\mathrm{T}}^2/2z\right)/\sqrt{R_{\mathrm{T}}}$ since the addition of a constant phase term does not change the focusing behaviour.

Given the separability highlighted in (2.15), the folding of the phase profile along the transverse radial coordinate $\rho_{\mathrm{T}}$ does not affect the helical phase front, thus orthogonality is preserved both at the transmitter and receiver sides. Indeed, accordingly to the previously-discussed model, each OAM state is uniquely identified by its topological charge $\ell_n$, affecting only the phase distribution along the azimuthal angle $\varphi_{\mathrm{T}}$; Consequently, any variation of the phase profile along the radial coordinate $\rho_{\mathrm{T}}$ does not entail any loss in terms of beams' separation.
The main drawback of this approach is that the distance among the antennas must be known at the transmitting side in order to focus the EM field. Nevertheless, this strategy requires phase-tapering only, i.e., the transmitting amplitude profile does not necessitate any further manipulation besides the additional exponential term reported in (4.10). As a consequence, the overall system complexity in the presence of focusing is in any case reduced with respect to optimum strategies.

When the phase profile (4.10) is considered, for the beam at the receiving LIS side we obtain

$$\begin{aligned}
\psi^{(n)}(\rho_{\mathrm{R}}, \varphi_{\mathrm{R}}, z) &= \frac{e^{-\jmath\kappa\frac{\rho_{\mathrm{R}}^2}{2z}}}{4\pi z\sqrt{2\pi R_{\mathrm{T}}}} \int_0^{R_{\mathrm{T}}}\int_0^{2\pi} e^{\jmath\ell_n\varphi_{\mathrm{T}}} e^{\jmath\kappa\frac{\rho_{\mathrm{R}}\rho_{\mathrm{T}}\cos(\varphi_{\mathrm{R}}-\varphi_{\mathrm{T}})}{z}} \rho_{\mathrm{T}}\,\mathrm{d}\varphi_{\mathrm{T}}\,\mathrm{d}\rho_{\mathrm{T}} \\
&= \frac{(-1)^{\ell_n}}{2z\sqrt{2\pi R_{\mathrm{T}}}} e^{-\jmath\kappa\frac{\rho_{\mathrm{R}}^2}{2z}} e^{\jmath\ell_n\varphi_{\mathrm{R}}} \int_0^{R_{\mathrm{T}}} \rho_{\mathrm{T}} J_{\ell_n}\left(\frac{\kappa\rho_{\mathrm{R}}\rho_{\mathrm{T}}}{z}\right) \mathrm{d}\rho_{\mathrm{T}}\,. 
\end{aligned} \tag{4.11}$$

Interestingly, (4.11) corresponds to the beam that would be obtained with the far-field (Fraunhofer) approximation, in spite of the fact that we are observing

the field within the Fresnel zone of the transmitting LIS. [1]
In fact, focusing along $\rho_\mathrm{T}$ compensates for the quadratic phase term responsible for the diffraction effects that are typical of the Fresnel zone, hence a more concentrated beam is obtained at the focal point. Notice that, when $\ell_n = 0$ (i.e., $n = 1$), we have

$$\begin{aligned}\psi^{(1)}(\rho_\mathrm{R}, \varphi_\mathrm{R}, z) =& \frac{1}{2z\sqrt{2\pi R_\mathrm{T}}} e^{-\jmath\kappa\frac{\rho_\mathrm{R}^2}{2z}} \int_0^{R_\mathrm{T}} \rho_\mathrm{T} J_0\left(\frac{\kappa\rho_\mathrm{R}\rho_\mathrm{T}}{z}\right) \mathrm{d}\rho_\mathrm{T} \\ =& \frac{\sqrt{R_\mathrm{T}}}{2\sqrt{2\pi}\kappa\rho_\mathrm{R}} e^{-\jmath\kappa\frac{\rho_\mathrm{R}^2}{2z}} J_1\left(\frac{\kappa\rho_\mathrm{R} R_\mathrm{T}}{z}\right) .\end{aligned} \tag{4.12}$$

The intensity profile coming from (4.12) is the classical far-field pattern of a circular aperture antenna (i.e., the *Airy disk* [47]). Remarkably, higher topological charges produce a beam divergence which is partially compensated by performing focusing.

## 4.2 Uncoded Transmissions on AWGN channels

Up to this point in our discussion, we neglected the presence of noise corruption in the data reception process. However, in order to render our theoretical system model as realistic and pertaining to real telecommunications systems as possible, random noise clearly cannot be omitted.
Indeed, an accurate description of the system's functioning and its relative performance evaluation requires the adoption of a suitable noise model that is able to properly mimic the effect of thermal noise and many other uncontrollable random processes that occur in nature, e.g., EM interference (EMI) coming from surrounding devices [48] or potential hardware impairments. These unwanted phenomena clearly have a non-negligible impact on the overall communication performance and are dependent on a number of parameters, which range from the specific antenna's implementation to the considered radio channel.

A truthful noise model to be adopted when in the presence of LISs should take into account the fact that, due to the spatial continuity of these aperture antennas, the noise samples that can be extrapolated by spatially sampling the received EM field cannot be assumed *a-priori* as Gaussian and independent, identically distributed (i.i.d.), as in classical communication theory. It is due to the fact that not only the transmitted, useful waveforms but also the noise of extrinsic nature associated with the EM wave need to satisfy the renowned Helmholtz equation, thus leading to spatial correlation; Note that this instead does not hold for the intrinsic thermal noise that is generated by the receiver. However, developing such a noise model and characterizing it appropriately

---

[1] This behaviour was also highlighted in [14, 46]

from the statistical point of view would require extensive and in-depth analysis that is beyond the scope of this thesis and will therefore be reserved for future works.

Concerning our specific case study, we will now refer to the simplest additive white Gaussian noise (AWGN) case, hence modeling any noise source of both intrinsic and extrinsic nature as a zero-mean ergodic Gaussian random process with a spatially white spectrum. Moreover, we will consider for simulation purposes discrete noise samples obtained by performing spatial sampling along each dimension of the receiving LIS at a spatial sampling interval $\Delta = \lambda/2$, according to the well-known Nyquist–Shannon sampling theorem. This operation translates into filtering the given noise realization with a low-pass filter of spatial bandwidth $W_S = 2\pi/(2\Delta) = 1/\lambda$ in the wavenumber frequency domain. Note that $1/\lambda$ corresponds to the free space wavenumber $\kappa_0 = 2\pi/\lambda$.[2] By performing sampling in adjacent points on the LIS antennas in this manner, the correlation between noise samples of any nature is subsequently eliminated.

Remarkably, the noise characterization that we have introduced is a simplified model used as a first approach to formalizing the communication problem, but when extending this analysis by taking into account external noise sources, a possible noise model to be adopted is the one presented in [49].

In particular, we are now assuming the presence of additive noise at the input of the correlation-based reception schemes, as reported in Figure 4.1, that is only a function of the considered signal-to-noise ratio (SNR) and antennas' sizes.

From the signal processing viewpoint, we are going to consider the following complex low-pass signal model henceforth:

$$\begin{aligned} \mathrm{y}(x,y,z) &= \psi(x,y,z) + \mathrm{n}(x,y) \\ &= \sum_{n=1}^{N} x_n \psi^{(n)}(x,y,z) + \mathrm{n}(x,y) \end{aligned} \tag{4.13}$$

where $x$ and $y$ are the coordinates on the receiving LIS's surface, $\mathrm{y}(x,y,z)$ identifies the received noisy signal, and $\psi(x,y,z)$ is the useful signal resulting from the superposition of the $N$ transmitted OAM modes. Moreover, $\mathrm{n}(x,y)$ represents a white, Gaussian, band-limited, random noise process with constant power spectral density (PSD) equal to $2N_0$ within the spatial bandwidth $W_S = 1/\lambda$.

Since in this treatise we are contemplating a polar reference system rather than a traditional Cartesian one, we can rewrite this model by performing a change of variable as:

---

[2] Noteworthily, due to the intrinsic nature of the communication problem under investigation, the traditional concept of signals that are defined in the time or, equivalently, in the frequency domain is discarded. Indeed, in our case, a mapping between the signals' temporal dimension and the spatial one holds, thus the notion of frequency is paralleled with that of corresponding to the wavenumber $\kappa$.

$$
\begin{aligned}
\mathrm{y}(\rho_{\mathrm{R}}, \varphi_{\mathrm{R}}, z) &= \psi(\rho_{\mathrm{R}}, \varphi_{\mathrm{R}}, z) + \mathrm{w}(\rho_{\mathrm{R}}, \varphi_{\mathrm{R}}) \\
&= \sum_{n=1}^{N} x_n \psi^{(n)}(\rho_{\mathrm{R}}, \varphi_{\mathrm{R}}, z) + \mathrm{w}(\rho_{\mathrm{R}}, \varphi_{\mathrm{R}}) \qquad (4.14)
\end{aligned}
$$

In this case, $\mathrm{w}(\rho_{\mathrm{R}}, \varphi_{\mathrm{R}})$ is a complex function in the radial and azimuthal coordinates that still represents a random noise process, but that is not white nor Gaussian anymore. Particularly, due to the fact that $\rho_{\mathrm{R}}$ and $\varphi_{\mathrm{R}}$ are interdependent variables, the bivariate noise distribution in polar coordinates is thus far unknown due to its complicated characterization and is still under our investigation.

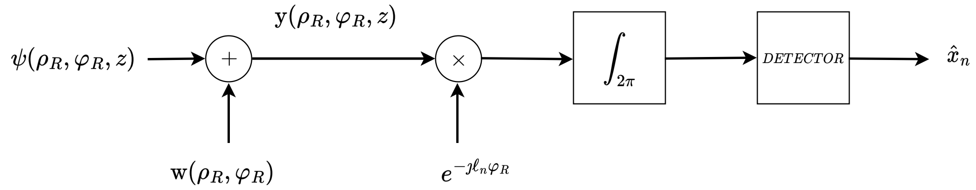

**Figure 4.1:** *Block diagram of the complete reception scheme in the presence of AWGN noise.*

Apart from that, we will restrict our study of the OAM-based transmission to the case of uncoded communications by reason of the immediateness of the treatise. Therefore, the transmitted symbols sequences of length $N$ are obtained by employing any arbitrary digital amplitude modulation, e.g., binary phase shift keying (BPSK) or on-off keying (OOK). Naturally, the modulation choice affects the overall system's architecture and performance; in particular, it affects the selection of the most convenient detection scheme to adopt, being dependent upon the modulation coherency, its dimensionality and order, and so on.
Besides this, due to the absence of any channel coding strategy, all the symbols' sequence combinations are possible, and we will assume them as equiprobable. In this manner, we ensure the complete independence of the $\{x_n\}$ symbols, thus obtaining that symbol-by-symbol detection is optimum and leads to the minimization of the bit error probability.

As regards the specific symbols' detection procedure, thanks to the helical wavefront propagating with no changes along the azimuthal coordinate, a correlation at the receiver side with a conjugate factor $e^{-\jmath \ell_n \varphi_{\mathrm{R}}}$ enables to isolate the $n$-th contribution from the overall received EM field (4.9). This process can be viewed as a matching operation performed at EM level. Formally, considering herein the OAM-multiplexed signal component only and neglecting the noise presence, we have

$$\begin{aligned}\int_0^{2\pi} \psi(\rho_\mathrm{R}, \varphi_\mathrm{R}, z) e^{-\jmath \ell_n \varphi_\mathrm{R}} \, \mathrm{d}\varphi_\mathrm{R} &= \int_0^{2\pi} \sum_{n=1}^{N} x_n \psi^{(n)}(\rho_\mathrm{R}, \varphi_\mathrm{R}, z) e^{-\jmath \ell_n \varphi_\mathrm{R}} \, \mathrm{d}\varphi_\mathrm{R} \\ &= \frac{(-1)^{\ell_n}}{2z\sqrt{2\pi R_\mathrm{T}}} e^{-\jmath\kappa \frac{\rho_\mathrm{R}^2}{2z}} e^{-\jmath\kappa z} x_n \int_0^{R_\mathrm{T}} \rho_\mathrm{T} e^{-\jmath\kappa \frac{\rho_\mathrm{T}^2}{2z}} J_{\ell_n}\left(\frac{\kappa \rho_\mathrm{R} \rho_\mathrm{T}}{z}\right) \mathrm{d}\rho_\mathrm{T} \\ &= x_n f_n(\rho_\mathrm{R}) \end{aligned} \tag{4.15}$$

where

$$f_n(\rho_\mathrm{R}) = \frac{(-1)^{\ell_n}}{2z\sqrt{2\pi R_\mathrm{T}}} e^{-\jmath\kappa \frac{\rho_\mathrm{R}^2}{2z}} e^{-\jmath\kappa z} \int_0^{R_\mathrm{T}} \rho_\mathrm{T} e^{-\jmath\kappa \frac{\rho_\mathrm{T}^2}{2z}} J_{\ell_n}\left(\frac{\kappa \rho_\mathrm{R} \rho_\mathrm{T}}{z}\right) \mathrm{d}\rho_\mathrm{T} \,. \tag{4.16}$$

At this point, different approaches could be employed to detect the transmitted symbol $x_n$, from the $n$-th EM field component $f_n(\rho_\mathrm{R})$ along the radial coordinate $\rho_\mathrm{R}$.

Above all, the optimum strategy for maximizing the energy at the $n$-th branch of the receiver is that of performing traditional matched filtering, i.e., computing the correlation also along the radial coordinate $\rho_\mathrm{R}$ with a function matched to (4.15). Thus, the decision variable $Y_n$ used for signal demodulation at the $n$-th branch is

$$\begin{aligned} Y_n &= \int_0^{R_\mathrm{R}} x_n f_n(\rho_\mathrm{R}) f_n^*(\rho_\mathrm{R}) \, \mathrm{d}\rho_\mathrm{R} + \int_0^{R_\mathrm{R}} \int_0^{2\pi} \mathrm{w}(\rho_\mathrm{R}, \varphi_\mathrm{R}) f_n^*(\rho_\mathrm{R}) e^{-\jmath \ell_n \varphi_\mathrm{R}} \, \mathrm{d}\varphi_\mathrm{R} \, \mathrm{d}\rho_\mathrm{R} \\ &= x_n \int_0^{R_\mathrm{R}} |f_n(\rho_\mathrm{R})|^2 \, \mathrm{d}\rho_\mathrm{R} + \int_0^{R_\mathrm{R}} \int_0^{2\pi} \mathrm{w}(\rho_\mathrm{R}, \varphi_\mathrm{R}) f_n^*(\rho_\mathrm{R}) e^{-\jmath \ell_n \varphi_\mathrm{R}} \, \mathrm{d}\varphi_\mathrm{R} \, \mathrm{d}\rho_\mathrm{R} \\ &= \frac{1}{8\pi z^2 R_\mathrm{T}} x_n \int_0^{R_\mathrm{R}} \left| \int_0^{R_\mathrm{T}} \rho_\mathrm{T} e^{-\jmath\kappa \frac{\rho_\mathrm{T}^2}{2z}} J_{\ell_n}\left(\frac{\kappa \rho_\mathrm{R} \rho_\mathrm{T}}{z}\right) \mathrm{d}\rho_\mathrm{T} \right|^2 \mathrm{d}\rho_\mathrm{R} \\ &\qquad + \int_0^{R_\mathrm{R}} \int_0^{2\pi} \mathrm{w}(\rho_\mathrm{R}, \varphi_\mathrm{R}) f_n^*(\rho_\mathrm{R}) e^{-\jmath \ell_n \varphi_\mathrm{R}} \, \mathrm{d}\varphi_\mathrm{R} \, \mathrm{d}\rho_\mathrm{R} \end{aligned} \tag{4.17}$$

This strategy corresponds to assuming a receiver basis set in the form $\psi_n(\rho_\mathrm{R}, \varphi_\mathrm{R}) = \psi_n^\rho(\rho_\mathrm{R}) \psi_n^\varphi(\varphi_\mathrm{R})$, where

$$\psi_n^\rho(\rho_\mathrm{R}) = f_n(\rho_\mathrm{R}) \tag{4.18}$$

$$\psi_n^\varphi(\varphi_\mathrm{R}) = e^{\jmath \ell_n \varphi_\mathrm{R}} \tag{4.19}$$

Unfortunately, such a strategy requires high complexity at the receiving LIS side. In fact:

- The correlation with a complex amplitude/phase pattern must be performed;

- The distance between transmitter and receiver, as well the transmitting LIS's size, must be known at the receiver side.

The equivalent processing scheme is reported in Figure 4.2. Naturally, when focusing is performed at the transmitting LIS, the quadratic phase term of $\rho_{\mathrm{T}}$ will not be included within the template function $f_n(\rho_{\mathrm{T}})$ in (4.16), being it pre-compensated in advance at the transmitting side.

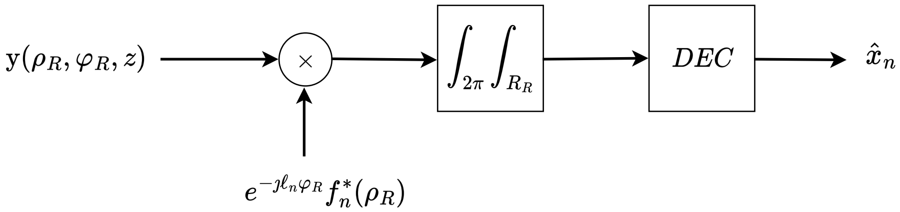

**Figure 4.2:** *Matched filtering processing scheme for OAM detection.*

With reference to our case of interest and subsequent numerical study, we will evaluate the matched filter performance by adopting as a digital modulation scheme a conventional BPSK, according to which the transmitted symbols can only take values $x_n = \pm 1$. As a consequence, assuming equiprobable symbols occurrence, the decision criterion that has been considered is the classical sign test that is performed on the sufficient statistics [50], which in our specific case coincides with the real part of the complex decision variable $Y_n$. Essentially, the decision rule that has been adopted can be summarized as follows:

$$\hat{x}_n = \begin{cases} +1, & \mathfrak{Re}\{Y_n\} \geq 0 \\ -1, & \mathfrak{Re}\{Y_n\} < 0 \end{cases} \tag{4.20}$$

Additionally, in accordance with the traditional results for uncoded binary transmission in AWGN, it can be shown that the bit error rate (BER) when matched filtering is employed can be computed as:

$$P_b = \frac{1}{2}\mathrm{erfc}\left(\sqrt{\mathrm{SNR}_n}\right) \tag{4.21}$$

where the $\mathrm{SNR}_n$ is the SNR related to the specific OAM mode under analysis. Particularly, $\mathrm{SNR}_n$ is related to the total SNR at the receiver and the fraction of energy corresponding to the $n$-th OAM mode as

$$\mathrm{SNR}_n = \mathrm{SNR}\frac{\int_0^{R_{\mathrm{R}}}\int_0^{2\pi}\left|\psi^{(n)}(\rho_{\mathrm{R}},\varphi_{\mathrm{R}},z)\right|^2 \mathrm{d}\varphi_{\mathrm{R}}\,\mathrm{d}\rho_{\mathrm{R}}}{\int_0^{R_{\mathrm{R}}}\int_0^{2\pi}\left|\psi(\rho_{\mathrm{R}},\varphi_{\mathrm{R}},z)\right|^2 \mathrm{d}\varphi_{\mathrm{R}}\,\mathrm{d}\rho_{\mathrm{R}}} \tag{4.22}$$

where

$$\mathrm{SNR} = \frac{\int_0^{R_\mathrm{R}} \int_0^{2\pi} \left|\psi(\rho_\mathrm{R}, \varphi_\mathrm{R}, z)\right|^2 \,\mathrm{d}\varphi_\mathrm{R}\, \mathrm{d}\rho_\mathrm{R}}{N_0} \tag{4.23}$$

In summary, the signals/noise models and the relative assumptions that have been introduced in this section are relevant for determining some useful performance metrics, e.g., the BER as a function of some parameters of interest, such as the SNR or the link distance, thus performing a complete system's performance evaluation, as will be presented in the next chapter.

## 4.3 Strategies for System's Complexity Reduction

Intuitively, the adoption of the optimal matched filtering approach will result in the maximum possible achievements in terms of successful transmissions and correct symbols detection. However, it should be remembered that this represents the best solution *theoretically* and does not takes into account any exterior or factual considerations, such as the design and implementation difficulties or unexpected propagation phenomena that might occur in real wireless environments. Consequently, it could be fruitful to identify additional reception schemes and stratagems that might be of more straightforward implementation in a physical communication system, thus constituting a suitable trade-off between system complexity and detection accuracy. A detailed overview of some practicable solutions is reported hereafter, together with a discussion on the analysis and simulation issues that arise, though not directly addressed in this work.

### 4.3.1 Accumulation

An alternative procedure with respect to matched filtering is to consider a sub-optimum but lower complexity processing strategy along the radial coordinate $\rho_\mathrm{R}$, e.g., by performing a simple accumulation. This approach corresponds to assuming a receiver basis set in the form $\psi_n(\rho_\mathrm{R}, \varphi_\mathrm{R}) = \psi_n^\rho(\rho_\mathrm{R})\psi_n^\varphi(\varphi_\mathrm{R})$, where

$$\psi_n^\rho(\rho_\mathrm{R}) = \Pi_{R_\mathrm{R}}(\rho_\mathrm{R}) \tag{4.24}$$

$$\psi_n^\varphi(\varphi_\mathrm{R}) = e^{\jmath \ell_n \varphi_\mathrm{R}} \,. \tag{4.25}$$

Specifically, we have

$$\begin{aligned} Y_n &= \int_0^{R_\mathrm{R}} \int_0^{2\pi} \mathrm{y}(\rho_\mathrm{R}, \varphi_\mathrm{R}, z) e^{-\jmath \ell_n \varphi_\mathrm{R}} \, \mathrm{d}\varphi_\mathrm{R} \, \mathrm{d}\rho_\mathrm{R} \\ &= \int_0^{R_\mathrm{R}} x_n f_n(\rho_\mathrm{R}) \, \mathrm{d}\rho_\mathrm{R} + \int_0^{R_\mathrm{R}} \int_0^{2\pi} \mathrm{w}(\rho_\mathrm{R}, \varphi_\mathrm{R}) e^{-\jmath \ell_n \varphi_\mathrm{R}} \, \mathrm{d}\varphi_\mathrm{R} \, \mathrm{d}\rho_\mathrm{R} \\ &= \frac{(-1)^{\ell_n} e^{-\jmath \kappa z}}{2z\sqrt{2\pi R_\mathrm{T}}} x_n \int_0^{R_\mathrm{R}} e^{-\jmath \kappa \frac{\rho_\mathrm{R}^2}{2z}} \int_0^{R_\mathrm{T}} \rho_\mathrm{T} e^{-\jmath \kappa \frac{\rho_\mathrm{T}^2}{2z}} J_{\ell_n} \left( \frac{\kappa \rho_\mathrm{R} \rho_\mathrm{T}}{z} \right) \mathrm{d}\rho_\mathrm{T} \mathrm{d}\rho_\mathrm{R} \\ &\qquad + \int_0^{R_\mathrm{R}} \int_0^{2\pi} \mathrm{w}(\rho_\mathrm{R}, \varphi_\mathrm{R}) e^{-\jmath \ell_n \varphi_\mathrm{R}} \, \mathrm{d}\varphi_\mathrm{R} \, \mathrm{d}\rho_\mathrm{R}. \end{aligned} \tag{4.26}$$

In this case, the quadratic phase factors can play a crucial role in determining both the output decision variable strength and its sign; hence a cautious adoption of this strategy must be considered.
In fact, differently from all the other detection strategies hereby illustrated, the lack of the square module operation in Equation (4.26) renders the complex output variable $Y_n$ utterly dependent on the multiplication of three terms: the transmitting quadratic phase factor, the receiving one, and the $\ell_n$-th order Bessel function. Depending on the sign of the resulting product, the decision criterion to be adopted when detecting the transmit symbol $x_n$ consequently changes.
In pursuance of clarity, a glimpse of the behavior of the Bessel functions as a function of $\rho_\mathrm{R}$ for different values of the topological charge is reported in Figure 4.3. It can be noted that odd OAM orders correspond to Bessel functions with odd symmetry, i.e., flipped with respect to the abscissa. At the same time, even topological charges lead to overlapped Bessel curves (see $\ell_n = \pm 2$) due to their even symmetry.

Again, a traditional BPSK modulation could be employed with this detection approach; as a consequence, the symbol-by-symbol detection criterion still consists in checking the sign of the decision variable as reported in (4.20). However, differing from the matched filter case, when focusing is not performed, the presence of the quadratic phase terms and the intrinsic behavior of the Bessel functions modifies the actual sign of $\mathfrak{Re}\{Y_n\}$. For this reason, a practical and simple stratagem could be adopted to maintain unchanged the well-known sign test for symbol detection, hence removing the need to reprogram the threshold-based device for sign identification. Specifically, given the knowledge at the receiver side of the theoretical $\psi_n(\rho_\mathrm{R}, \varphi_\mathrm{R}, z)$ wave functions, a former check on the product of the three terms in (4.26) that are responsible for the Fresnel diffraction can be performed; hence a sign adjustment can be applied by pre-multiplying $Y_n$ by ±1 and, subsequently, comparing the resulting value with the decision threshold that is set to zero. This operation concretely translates into flipping the traditional decision criterion and counterintuitively selecting the opposite, e.g., select $x_n = +1$ when $Y_n < 0$ holds.
In light of this fact, a beneficial result for this sub-optimum detection strategy can be obtained by performing focusing both at the transmitting and receiving

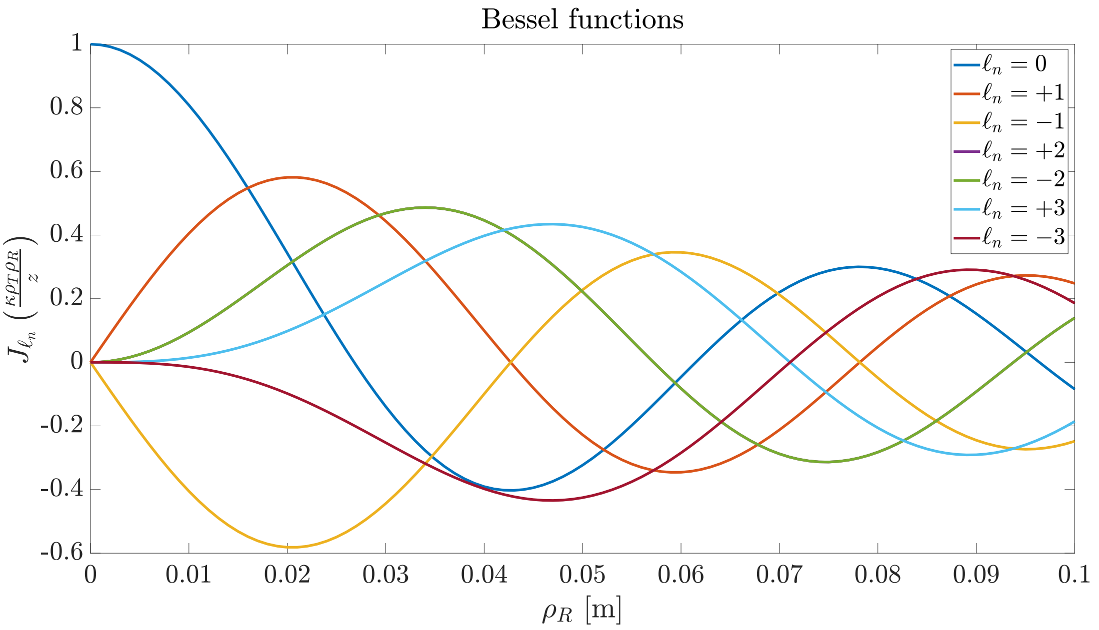

**Figure 4.3:** *Plot of the Bessel functions' terms included in Equation* (4.26) *as a function of* $\rho_R$ *for different topological charges* ($N = 7$).

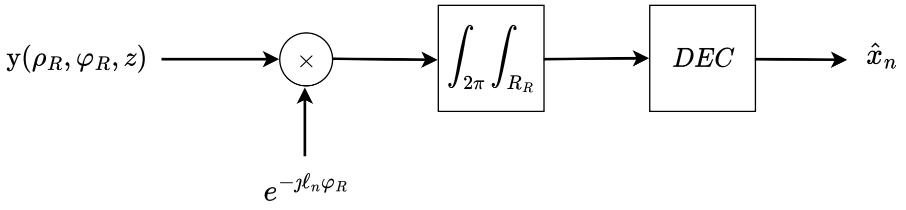

**(a)** *Accumulation.*

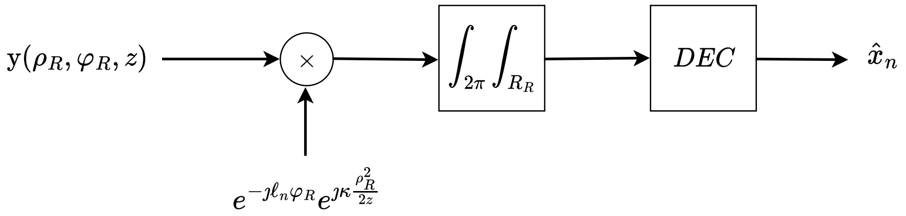

**(b)** *Accumulation with focusing.*

**Figure 4.4:** *Accumulation-based processing schemes for OAM detection.*

sides, thus compensating for the quadratic phase terms of $\rho_{\mathrm{T}}$ and $\rho_{\mathrm{R}}$ equally and eliminating the consequent $Y_n$ dependence on them. The equivalent processing schemes are reported in Figure 4.4a and Figure 4.4b.

Nonetheless, despite its apparent effortlessness, accumulation has a great disadvantage, i.e., it heavily suffers from noise enhancements that are intrinsically related to the specific OAM beams' amplitude patterns. Indeed, by collecting the energy impinging on the receiving LIS from all the $(\rho_\mathrm{R}, \varphi_\mathrm{R})$ locations, the receiver accumulates a massive amount of noise from those points where the useful signals' strength falls flat, if not optimized to perform the correlation only where it is meaningful to do so. As a solution to this, a cautious selection of the integration interval in the radial coordinate has to be effectuated, e.g., by employing a smart integration algorithm.

### 4.3.2 Smart Integration

In the previous section, it has emerged how, after performing a first correlation of the total received EM field with the conjugate phase factor $e^{-\jmath \ell_n \varphi_\mathrm{R}}$ of the mode of interest to be demultiplexed, integration in the variable $\rho_\mathrm{R}$ always need to be performed; this holds regardless of the adopted detection strategy or system configuration.
Intuitively, when the matched filtering scheme is employed at the receiver side and in the presence of Gaussian noise, this operation contributes to maximizing the SNR at the receiving LIS, being the selected receiver basis functions $\psi_n(\rho_\mathrm{R}, \varphi_\mathrm{R})$ perfectly adapted to the transmitted waveforms.[3] In this way, most of the unwanted propagation effects are equalized, as well as the amount of noise collected by the receiving antenna is significantly diminished.
However, when accumulation or further sub-optimum strategies are contemplated, the absence of any radial basis component $\psi_n^\rho(\rho_\mathrm{R})$ that is exactly matched to the received field radial function $f_n(\rho_\mathrm{R})$ might lead to noticeable performance degradation. This is because, when integrating along the totality of the receiving LIS's surface, i.e., $\rho_\mathrm{R} \in [0, R_\mathrm{R}]$, not only a fraction of the useful OAM waves' energy is collected, but also a consistent amount of noise is embedded, which comes from those locations on the receiving antenna where the field intensity $|f_n(\rho_\mathrm{R})|^2$ has negligible values.

To counteract this undesired phenomenon, a useful expedient to employ is that of performing the integral in $d\rho_\mathrm{R}$ only where the received EM field has a considerable intensity, e.g., above a predefined threshold, though eliminating the harmful noise enhancement coming from the irrelevant locations on the receiving LIS. This operation has been entitled as *smart integration* since we assume to have an intelligent receiving device that, given the knowledge of the OAM order that has been demultiplexed, is capable of identifying a suitable interval of $\rho_\mathrm{R}$ values on which perform the integration operation. Precisely, in analogy to the case of focused beams, such a strategy requires the receiver's knowledge of the system's geometry, i.e., the link distance and the transmitting antenna size, so that it can compute locally an estimation of the theoretic

---

[3] Note that this is not generally true when noise cannot be assumed as AWGN. In this case, the optimal reception scheme requires the knowledge of the specific noise distribution [51].

OAM signal waveform $\psi^{(n)}(\rho_\mathrm{R}, \varphi_\mathrm{R}, z)$ that is expected. Admittedly, this partially withdraws the advantages in terms of ease of implementation of those sub-optimum strategies; however, with this supplementary stratagem, there is no need to perform a correlation with a complex amplitude/phase profile as in the optimum detection case, but only a rapid test on the signal strength, e.g., via an additional threshold-based device.

Naturally, due to the completely different processing performed, the noise enhancements greatly vary depending on the specific detection strategy that has been adopted, the SNR, the considered OAM order, and several other elements. Consequently, the optimal threshold definition that establishes whether the beams' strength is greater than its noise counterpart changes, and the best integration interval needs to be determined based on the expected signal waveform and its energy distribution. For this reason, a unique, universally valid algorithm has still to be identified and will be left to further investigations.
Notably, several approaches have been proposed to tackle the identification of the proper length of the integration interval in the case of non-coherent reception schemes. For instance, [52, 53] designed a blind algorithm, dubbed as *stop-and-go*, that exploits in different contexts information theoretic criteria for model order selection and is able to identify the best integration interval without any *a-priori* channel state information.
For the sake of simplicity, we will limit our analysis to the exploitation of the OAM beams' amplitude profiles knowledge, and a brief description of the implementation steps of a feasible smart integration procedure is hereby reported. Firstly, an adequate value for the beam's intensity threshold $\gamma$ is arbitrarily selected based on the system's configuration and the presence/absence of focusing. Subsequently, for each OAM mode, the receiver computes the theoretical waveform $\psi^{(n)}(\rho_\mathrm{R}, \varphi_\mathrm{R}, z)$ and identifies its maximum value (global maximum) in $\rho_\mathrm{R} \in [0, R_\mathrm{R}]$. Afterward, the difference between this maximum and the absolute value of the threshold is calculated, thus obtaining the ordinates where the beam's intensity can be considered satisfactory. Last, the $\rho_\mathrm{R}$ values in correspondence of these two points, i.e., $\rho_{R_1}$ and $\rho_{R_2}$, are used as extremes of the integration interval; hence integration in $d\rho_\mathrm{R}$ is performed.
It should be noted that this intensity check needs to be performed compulsorily on the theoretical, noiseless waveforms because any small oscillation caused by thermal noise might lead to a malfunction of the overall procedure, e.g., by running into local maxima/minima that are the result of the AWGN random process and do not reflect the true amplitude profile of the OAM beams.

Intuitively, the consequences of employing smart integration reflect on the analytical formula of the decision variable as well. For instance, when accumulation is employed, the $Y_n$ expression reported in (4.26) becomes equal to

$$
\begin{aligned}
Y_n &= \int_{\rho_{R_1}}^{\rho_{R_2}} \int_0^{2\pi} \mathrm{y}(\rho_\mathrm{R}, \varphi_\mathrm{R}, z) e^{-\jmath \ell_n \varphi_\mathrm{R}} \, \mathrm{d}\varphi_\mathrm{R} \, \mathrm{d}\rho_\mathrm{R} \\
&= \int_{\rho_{R_1}}^{\rho_{R_2}} x_n f_n(\rho_\mathrm{R}) \, \mathrm{d}\rho_\mathrm{R} + \int_{\rho_{R_1}}^{\rho_{R_2}} \int_0^{2\pi} \mathrm{w}(\rho_\mathrm{R}, \varphi_\mathrm{R}) e^{-\jmath \ell_n \varphi_\mathrm{R}} \, \mathrm{d}\varphi_\mathrm{R} \, \mathrm{d}\rho_\mathrm{R} \\
&= \frac{(-1)^{\ell_n} e^{-\jmath \kappa z}}{2z\sqrt{2\pi R_\mathrm{T}}} x_n \int_{\rho_{R_1}}^{\rho_{R_2}} e^{-\jmath \kappa \frac{\rho_\mathrm{R}^2}{2z}} \int_0^{R_\mathrm{T}} \rho_\mathrm{T} e^{-\jmath \kappa \frac{\rho_\mathrm{T}^2}{2z}} J_{\ell_n}\left(\frac{\kappa \rho_\mathrm{R} \rho_\mathrm{T}}{z}\right) \mathrm{d}\rho_\mathrm{T} \mathrm{d}\rho_\mathrm{R} \\
&\qquad + \int_{\rho_{R_1}}^{\rho_{R_2}} \int_0^{2\pi} \mathrm{w}(\rho_\mathrm{R}, \varphi_\mathrm{R}) e^{-\jmath \ell_n \varphi_\mathrm{R}} \, \mathrm{d}\varphi_\mathrm{R} \, \mathrm{d}\rho_\mathrm{R}. \qquad (4.27)
\end{aligned}
$$

Evidently, depending on the choice of $\rho_{R_1}$ and $\rho_{R_2}$, the interplay between the useful waveform's component and its noise counterpart subsequently varies. Therefore, it emerges the necessity of optimizing not only the decision threshold selection but also the integration interval $[\rho_{R_1}, \rho_{R_2}]$ for every OAM mode depending on its specific energy distribution.

### 4.3.3 Energy Detection

In order to maximize the output energy without additional complexity at the receiving LIS, a simple energy detection can be performed. Thus, we have

$$
\begin{aligned}
Y_n &= \int_0^{R_\mathrm{R}} \int_0^{2\pi} \left| \mathrm{y}(\rho_\mathrm{R}, \varphi_\mathrm{R}, z) e^{-\jmath \ell_n \varphi_\mathrm{R}} \right|^2 \, \mathrm{d}\varphi_\mathrm{R} \, \mathrm{d}\rho_\mathrm{R} \\
&= \int_0^{R_\mathrm{R}} \int_0^{2\pi} \left| \sum_{n=1}^{N} x_n \psi^{(n)}(\rho_\mathrm{R}, \varphi_\mathrm{R}, z) e^{-\jmath \ell_n \varphi_\mathrm{R}} + \mathrm{w}(\rho_\mathrm{R}, \varphi_\mathrm{R}) e^{-\jmath \ell_n \varphi_\mathrm{R}} \right|^2 \, \mathrm{d}\varphi_\mathrm{R} \, \mathrm{d}\rho_\mathrm{R}
\end{aligned}
\qquad (4.28)
$$

so that all the energy along the radial component $\rho_\mathrm{R}$ is collected.
For this detection strategy, focusing at the transmitting LIS is beneficial to minimize the beam widening; on the contrary, no improvement is given by performing focusing at the receiving LIS. By way of illustration, an insight into the equivalent processing scheme is reported in Figure 4.5.
Conversely to the other detection strategies, energy detection cannot be realized with the general communication scheme of Figure 2.2, since integration over the angular coordinate $\varphi_\mathrm{R}$ only is required and, afterward, processing the energy along the radial coordinate $\rho_\mathrm{R}$ has to be performed.

Differently from the matched filter and the accumulation reception schemes, the square module operation performed by this detector before computing the correlation integral along the radial direction $\rho_\mathrm{R}$ has several non-negligible consequences:

- Due to the presence of the square law device in the reception scheme, any information regarding the signal's phase is lost, thus rendering any

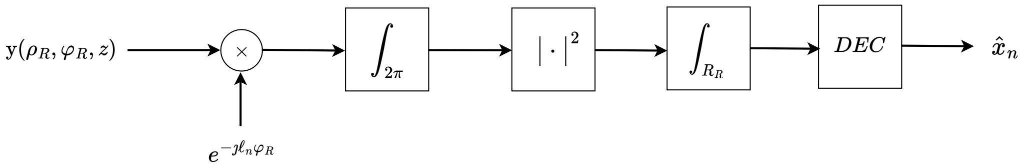

**Figure 4.5:** *Energy detection-based processing scheme for OAM detection.*

coherent modulation technique totally ineffective. For instance, in the case of BPSK, it would be impossible to distinguish whether the transmitted symbol was $x_n = +1$ or $x_n = -1$. For this reason, non-coherent modulation schemes only must be adopted. In the followings, we will assume that the energy detector employs a traditional OOK modulation, under which the symbols can have values equal to $x_n = 0$ or $x_n = +1$, and we will assume them as equiprobable once again.

- It can be shown that the statistics of the decision variable $Y_n$ cannot be assumed to have the same probability distribution of noise anymore, as it typically occurs with the most widely known detection schemes. Indeed, if the noise input is Gaussian and has a flat, band-limited power density spectrum, it can be demonstrated that the energy that is collected by the receiver in a finite region can be well approximated by the sum of the square of a given number of statistically independent Gaussian variates [54].
  Without entering into the statistical description of our reference case, this detection scheme basically leads to two different outcomes: a first case in which the decision variable $Y_n$ is composed of the noise energy only, and a second one in which $Y_n$ comprises both the transmitted signal and the noise energies. Consequently, the final symbol's decision can be performed by comparing the energy level measured at the energy detector's output with an appropriate threshold value. Therefore, the decision criterion that could be adopted when in the presence of an OAM-based transmission is the following:

$$\hat{x}_n = \begin{cases} +1 & , Y_n \geq \zeta_n \\ 0 & , Y_n < \zeta_n \end{cases} \tag{4.29}$$

  where $\zeta_n$ identifies the decision threshold that has been suitably defined for the $n$-th OAM mode.
  For comparison, when considering the occurrence of noisy signals in the time domain, the performance characterization of the energy detection scheme can be obtained by analyzing the specific decision variable's statistics. Particularly, in the case of noise only (i.e., $x_n = 0$), the output

of the energy detector has been proved in [54] to have a central chi-square distribution with a number of DoFs equal to twice the time-bandwidth product at its input. Similarly, when in the presence of a deterministic signal (i.e., $x_n = +1$), though its form might be unknown, the distribution of $Y_n$ at the output of the detector is that of a non-central chi-square distribution with the number of DoFs equal to twice the time-bandwidth product and a non-centrality parameter given by the SNR of the specific OAM mode that is being detected (i.e., $\mathrm{SNR}_n$).

- Since an energy detector does not account for anything else outside the portion of energy that is collected in a given signal's observation interval, the EM field distribution in space and the selected signals' shape do not affect the conditional probability that a given threshold will be exceeded when the signal is present. However, the identification of the optimal threshold according to which detection is performed is not straightforward, thus representing another critical point of this discussion.
  Specifically, let us consider the following hypothesis testing problem:

$$\begin{cases} H_0: & \mathrm{y}_n(\rho_\mathrm{R}, \varphi_\mathrm{R}, z) = w_n(\rho_\mathrm{R}, \varphi_\mathrm{R}) \\ H_1: & \mathrm{y}_n(\rho_\mathrm{R}, \varphi_\mathrm{R}, z) = x_n \psi^{(n)}(\rho_\mathrm{R}, \varphi_\mathrm{R}, z) + w_n(\rho_\mathrm{R}, \varphi_\mathrm{R}) \end{cases} \tag{4.30}$$

  where $\mathrm{y}_n(\rho_\mathrm{R}, \varphi_\mathrm{R}, z)$ and $w_n(\rho_\mathrm{R}, \varphi_\mathrm{R})$ represent, respectively, the $n$-th received signal component and the relative noise realization in correspondence of the OAM communication mode of order $\ell_n$. It should be noted that (4.30) does not constitute a traditional waveforms' binary detection problem because the only quantity of interest for detection purposes is the value of the scalar variable $Y_n$, which is obtained via measuring the input's energy.
  Since the probability density functions (p.d.f.s) corresponding to the two hypotheses, hence their relative $Y_n$ variables, are not Gaussian but rather have two completely different statistics, the optimal detection threshold is far from the one defined as per classical decision theory [55]. Particularly, the optimal threshold in an energy detector receiver depends on several elements, such as the noise variance, the received signal energy, the integration interval, and the specific noise filtering technique that is adopted. Therefore, no closed-form expression for threshold determination can be found in the literature. However, its value could be found by iteratively solving an equation that minimizes the error probability [56], or via an asymptotic approximation of the modified Bessel function of the first kind holding under high SNR assumption [57], or again by introducing a Gaussian approximation for the p.d.f.s when the number of DoFs grows large (i.e., the central limit theorem applies).

- Being the square module a non-linear operation, the presence of undesired non-linear effects on the detector's output must be taken into account. Particularly, these effects become critical in relation to Gaussian noise, which is known for having a white, frequency-flat spectrum.

> Non-linearities can give rise to undesired spectral components and intermodulation products which may fall within the signal's band of interest, hence causing signals' distortion and interference. For this reason, it is good practice to always put before the square law device a band-pass filter centered on the carrier frequency of the transmitted waveform to eliminate out-of-band noise.[4]

Concerning our OAM case study, the threshold determination process could advantageously exploit the knowledge at the receiving LIS side of the theoretical $\psi^{(n)}(\rho_{\mathrm{R}}, \varphi_{\mathrm{R}}, z)$ waveforms. Specifically, the rationale behind its calculation is computing the average energy collected under hypothesis $H_0$ and the energy in the $H_1$ case, respectively. Given these values, their difference can be computed, and the threshold can finally be set in the middle of this energy range. Moreover, this procedure can be performed for every OAM mode of interest so that to obtain an ad-hoc threshold value adapted to the average noise power, i.e., $[\zeta_1, \zeta_2, \ldots, \zeta_N]$. Intuitively, this is a pretty coarse approximation, i.e., set the decision threshold $\zeta$ at the center of the energy range identified by the energy of the $x_n = 1$ case and the one of the $x_n = 0$ respectively. Admittedly, this solution is sub-optimal compared to the aforementioned threshold determination strategies, though being pretty effective in capturing, hence displaying, the energy detector performance.

Differently from the other two detection schemes, the closed-form analytical expression for the BER cannot be derived straightforwardly, being its exact value conditioned to the decision threshold choice, the number of DoFs and the SNR. Moreover, depending on whether the receiver has partial or complete knowledge of the transmitted waveform or the useful signal has a total unknown distribution, only approximate formulas can be found concerning the specific scenario that is considered and its assumptions. Due to this, it is unlikely that a closed-form expression for the bit error probability can be found, thus requiring the introduction of some approximations. For this reason, we leave such complex investigation to future works.

Lastly, it can be noted that, in analogy with the accumulation case, adopting smart integration with the energy detector could be beneficial in reducing the errors' occurrence. This result can appear counterintuitive since one might think that the larger amount of energy that is collected by the receiver, the easier it will be to perform a correct detection. However, this holds only if the signal's energy is substantially larger than its noise counterpart while the observation interval, i.e., the integration range, increases. If this does not hold, it is convenient to perform the integration only in correspondance of the receiving antenna's locations where the signal is much stronger than the noise compo-

---

[4] Although we are contemplating conventional EM fields that are emitted at radio frequencies, in our study, we always refer to the complex envelope of the EM field. Indeed, we are analyzing the spatial distribution of a complex function of bandwidth $W_S = 1/\lambda$ on a plane, which corresponds to a bi-dimensional, complex low-pass signal centered on a frequency $f_0$.

nent. Unfortunately, this is not the case for the OAM waveforms. Indeed, both with pencil-sharpened beams or with unfocused ones, the received field amplitude tends to be concentrated on a given $\rho_\mathrm{R}$ interval, hence rapidly vanishing outside of it; therefore, integrating where the OAM modes have very exiguous intensities will result in collecting larger amounts of noise, thus entailing an unavoidable deterioration of the receiver's detection capabilities.

# Chapter 5

# Numerical Study

In this chapter, a numerical analysis is presented in order to characterize the previous results, thus facilitating the reader's understanding and visualization of the benefits and disadvantages of this OAM-based transmission technique.

Concerning the general antennas' layout, consider two parallel, circular LISs placed at distance $z = D\lambda$ and arranged as previously illustrated in Figure 2.3. Moreover, the transmitting LIS is assumed to have a radius equal to $R_{\mathrm{T}} = T\lambda$, while the receiving LIS has a radius $R_{\mathrm{R}} = R\lambda$.

## 5.1 Simulation Setup

To perform the numerical simulations that will be discussed next, the programming computing platform named Matlab has been used.
In particular, the activity comprised the development of ad-hoc Matlab scripts that, firstly, model the target LISs-based system and then perform several semi-analytical Monte Carlo simulations to evaluate its performance.
By following the order of the various code blocks that compose our simulation environment, we first defined the system's geometry and initialized its relative parameters. Where it is not explicitly stated, the adopted parameters' values have been set as follows:

- $c = 3 \times 10^8\ m/s$ (free-space is assumed)
- $\lambda = 1$ cm (i.e., millimeter wave range)
- $f_0 = 28 \times 10^9$ Hz (carrier frequency)
- $T = R = 10$ (i.e., $R_{\mathrm{T}} = R_{\mathrm{R}} = 10\lambda$)
- $D = 30$ (i.e., $z = 30\lambda$)
- $\Delta_T = \frac{\lambda}{4}$ (transmitting antenna discretization step in $xy$ coordinates)
- $\Delta_R = \frac{\lambda}{4}$ (receiving antenna discretization step in $xy$ coordinates)

The discretization steps that are hereby reported have been introduced in order to ideally fragment both LISs and compute numerically the integrals that lead to the desired OAM waveforms. It is important to mention that a careful selection of these specific parameters has to be made since too large discretization steps might not accurately model the system under analysis, thus leading to the distortion of the simulated OAM beams and the complete failure of our numerical model. However, too small discretization steps might imply a huge, perhaps unnecessary, computation overhead and simulation time, hence a suitable trade-off between the simulations' reliability and the computational burden has to be identified.

Note that due to our specific implementation choice and other programming constraints, e.g., the fact that MATLAB environment can only work with vectors, matrices, and similar data types, the modeling of a circular LIS entailed the creation of a square surface antenna first and, afterward, the setting of all the matrix's elements falling outside the circular aperture of interest equal to zero.

Subsequently, we derived the received OAM-multiplexed field by computing various numerical integrals according to Equations (4.8)-(4.11). At this point, we set up the additional parameters to evaluate the BER as a function of the SNR or the link distance, that is:

- $N\_MonteCarlo = 10^5$ (i.e., the number of Monte Carlo cycles for noise generation or, equivalently, the number of symbols to be transmitted)
- SNR$_dB_values = [0, 2, 4, 6, 8, 10, 12, 14, 16, 18, 20]$ dB (i.e., the various SNR steps to evaluate)
- $D = [5, 10, 20, 30, 40, 50, 60, 70, 80, 90]$ (i.e., the link distances $z$ to test)

After that, the noise PSD value $N_0$ is obtained by fixing the SNR and calculating the total waveform energy $E_{TOT} = \int_0^{R_\mathrm{R}} \int_0^{2\pi} |\psi(\rho_\mathrm{R}, \varphi_\mathrm{R}, z)|^2 \, \mathrm{d}\varphi_\mathrm{R} \, \mathrm{d}\rho_\mathrm{R}$, hence inverting Equation (4.23); then, we simulated an uncoded binary transmission. Here we implemented the matched filter detection as illustrated in Chapter 4, hence a BER estimation based on the number of errors committed by the receiver is provided.

Finally, the last section of the code is devoted to the generation of the results' plots, as reported hereafter, and to the figurative comparison with closed-form BER formulas.

## 5.2 Received EM Field

Figure 5.1 shows the amplitude of the radial component of the received electric field (i.e., $|f_n(\rho_\mathrm{R})|$) considering the geometry defined in the previous section. It can be noticed that the beam divergence increases for higher values of the topological charge $\ell_n$. Moreover, the beam widening effect is visible due to the received EM field's observation within the Fresnel zone. In fact, within the numerical setup chosen, the boundary between near field and far field $D_\mathrm{ff}$, in

terms of multiple of the wavelength $\lambda$, is $D_{\mathrm{ff}} = 8T^2$ ($D_{\mathrm{ff}} = 800 > D$ in the proposed numerical example).
In contrast, when considering focusing at the transmitter side according to (4.10) with the same system configuration, the amplitude of the radial component of the received electric field (i.e., $|f_n(\rho_{\mathrm{R}})|$) is that as reported in Figure 5.2. The focusing effect is clearly visible, producing much more concentrated beams, thus maximizing the energy which can be collected by the receiving LIS. Having compensated the quadratic terms at the transmitter side, which produces the near-field beam widening effect, the beam divergence is evidently observable. Intuitively, a receiving LIS is consequently much more efficient than a UCA in collecting the energy for different topological charges, thanks to its continuity in space.

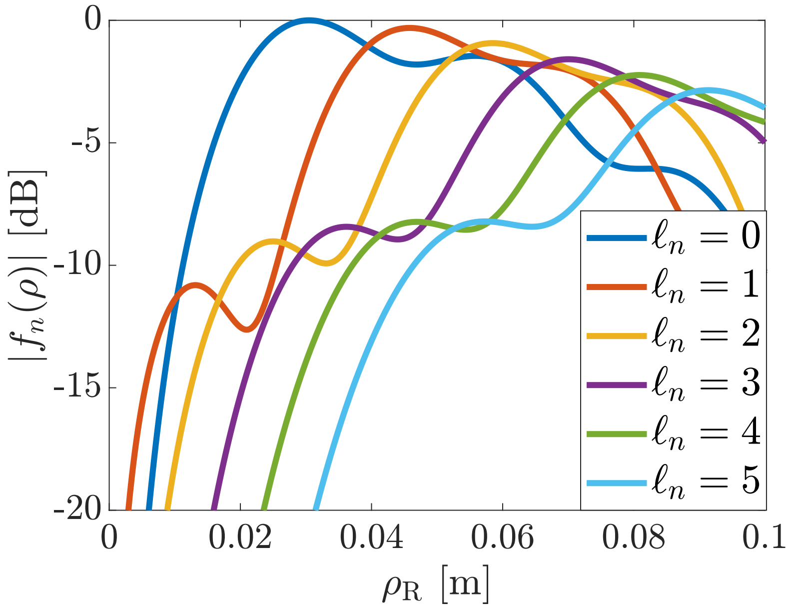

**Figure 5.1:** *Received EM field along the radial coordinate* $\rho_{\mathrm{R}}$ *for different topological charges* $\ell_n$ *(normalized to* $\max\{|f_0(\rho_{\mathrm{R}})|\}$*).*

Examples of the phase profiles at the transmitting LIS and the beams (both amplitude and phase distributions) obtained at the receiving LIS for different topological charges are reported in Figure 5.3, either in the presence or in the absence of focusing at the transmitter.
In particular, results for $\ell_n = 0$ (first row) are the beams obtained with unfocused/focused constant phase profiles along $\varphi_{\mathrm{T}}$, thus corresponding to classical diffraction patterns of circular apertures. The increasing beam divergence, partially compensated by focusing, can be seen in the subsequent rows for increasing values of $\ell_n$, as well as the corresponding helical-shaped phase profiles at receiver side.

To better visualize the EM field distribution in space, Figure 5.4 and Figure 5.5 depict the three dimensional total received field $\psi(\rho_{\mathrm{R}}, \varphi_{\mathrm{R}}, z)$ resulting

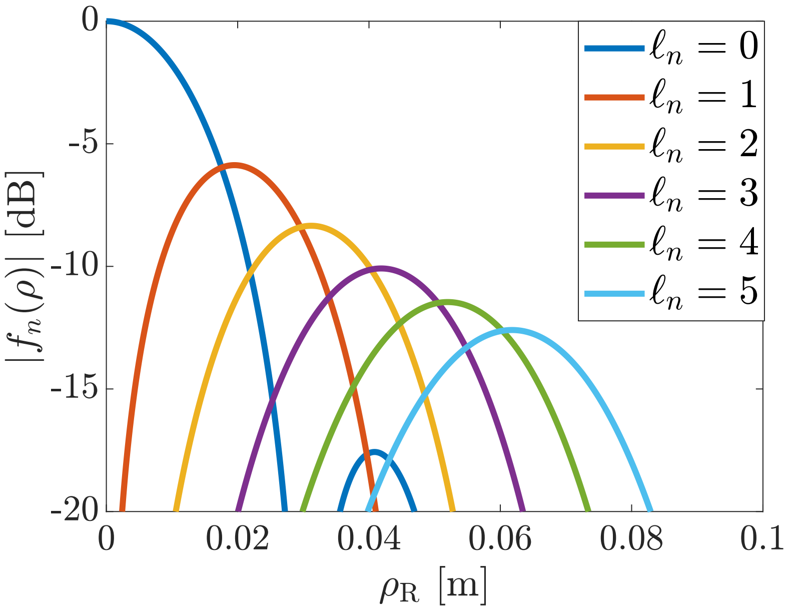

**Figure 5.2:** *Received EM field along the radial coordinate* $\rho_{\mathrm{R}}$ *for different topological charges* $\ell_n$ *using focusing at the transmitter side (normalized to* $\max\{|f_0(\rho_{\mathrm{R}})|\}$*).*

from the superposition of the different OAM beams. In particular, the former illustrates the received field distribution when focusing, i.e., the quadratic phase terms compensation is performed both at the transmitter and the receiver. Again, the typical behavior of the Bessel functions is easily observable. However, it should be noted that when performing focusing at the transmitting side, the presence of multiple, closely located maxima in the neighborhood of the receiving antenna center is assured. In that way, most of the transmitted power, i.e., that of is carried by the well-coupled, lower orders OAM waves, is collected from the receiving LIS.

In opposition, when focusing is not performed (Figure 5.5), the only maximum that stands out is the one corresponding to the mode that is not carrying OAM, i.e., $\ell_n = 0$; the higher orders beams instead are heavily attenuated due to the wavefronts' divergence phenomenon, alongside the ineluctable free-space path loss affecting all the propagating modes.

Finally, in Figure 5.6 the amplitude of the single EM field components $\left|\psi^{(n)}(\rho_{\mathrm{R}}, \varphi_{\mathrm{R}}, z)\right|$, whose superposition gives rise to the total field distribution in Figure 5.4, is displayed both for the focused and unfocused case. The presence of the phase singularity, typical of the OAM vortices, and the divergence phenomenon is evidently observable in all beams provided with angular momentum, while in the case of the plane wave carrying only SAM, i.e., $\ell_n = 0$ mode, the amplitude distribution resembles the well-known shape of the Bessel function of order zero.

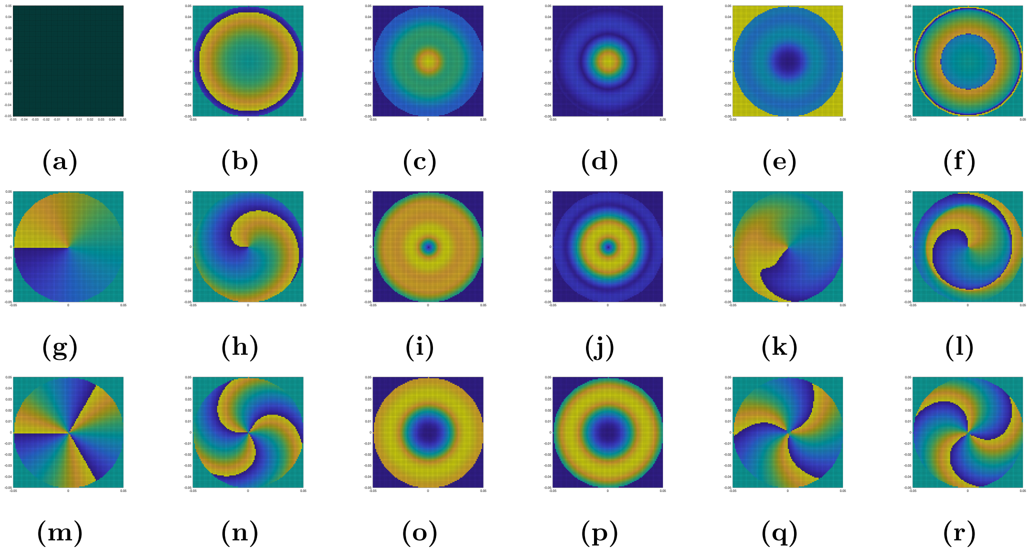
(a) (b) (c) (d) (e) (f)
(g) (h) (i) (j) (k) (l)
(m) (n) (o) (p) (q) (r)

**Figure 5.3:** *Example of transmitting and receiving amplitude/phase profiles, with and without focusing, for* $\ell_n = 0$ *(first line),* $\ell_n = +1$ *(second line), and* $\ell_n = +3$ *(third line). The first and second columns refer respectively to the unfocused and focused phase profiles at the transmitter, while the third and fourth columns represent the received field amplitudes for the unfocused and focused case. The last two columns correspondingly depict the received phase profiles without and with focusing* ($T = R = 5$, $D = 20$)*.*

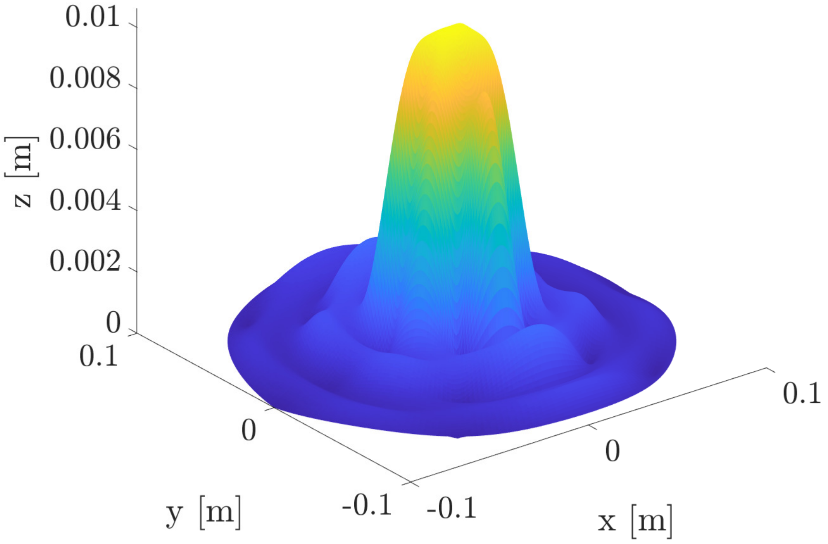

**Figure 5.4:** *EM field distribution on the receiving LIS when focusing is performed both at the transmitter and the receiver at* $D = 30$*.*

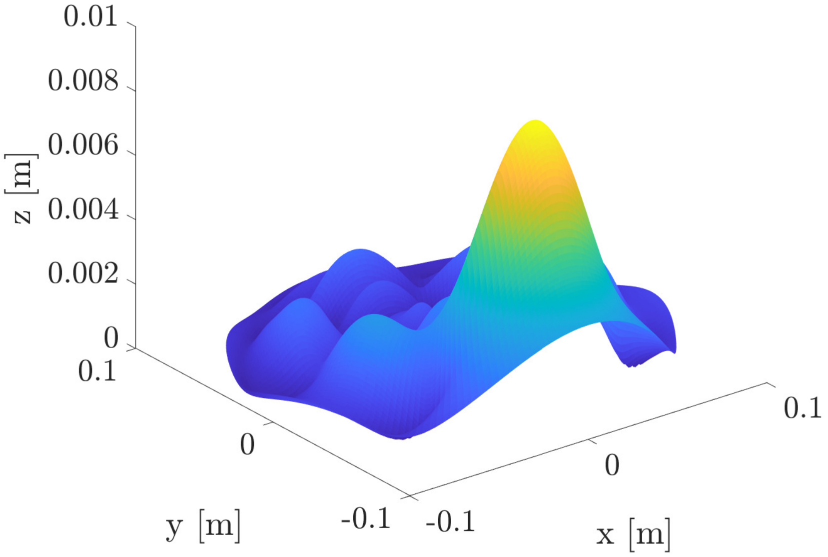

**Figure 5.5:** *Unfocused EM field distribution on the receiving LIS, with the global maximum corresponding to the fundamental mode ($\ell_n = 0$) at $D = 30$.*

## 5.3 Degrees of Freedom

We now compare the coupling intensity obtained with OAM with the coupling intensity obtained from the optimum bases (i.e., the intensity of the singular values $\xi_n$ coming from the definition of communication modes). The latter ones are obtained by discretizing the transmitting and receiving LISs, then computing the singular value decomposition (SVD) of the Green function as per (2.3) between the surfaces. In Figure 5.7 the behavior of singular values is reported. It can be seen that they are almost constant, then drop quickly after a specific value.

From a concrete viewpoint, the number of effective communication modes can be defined as the number of singular values of intensity no smaller than a certain value, i.e., the selected threshold, with respect to the largest one.

The coupling intensity of the OAM modes corresponds to the values of the decision variable $|Y_n|^2$ (normalized by their maximum) in the absence of noise for the matched filtering or energy detection cases (i.e., (4.17) or (4.28)), presenting the same energy output. As anticipated, OAM-based modes are degenerate, hence the same coupling is consequently obtained for two consecutive indexes $n$, except for the case $n = 1$ (i.e., $\ell_n = 0$).

Due to the beam divergence presence, OAM-based modes coupling falls off quite rapidly compared to the optimal case. However, it can be noticed how beneficial the adoption of focusing techniques is in terms of coupling strength. In this setup, by fixing a threshold to $-5\,\mathrm{dB}$ from the best-connected com-

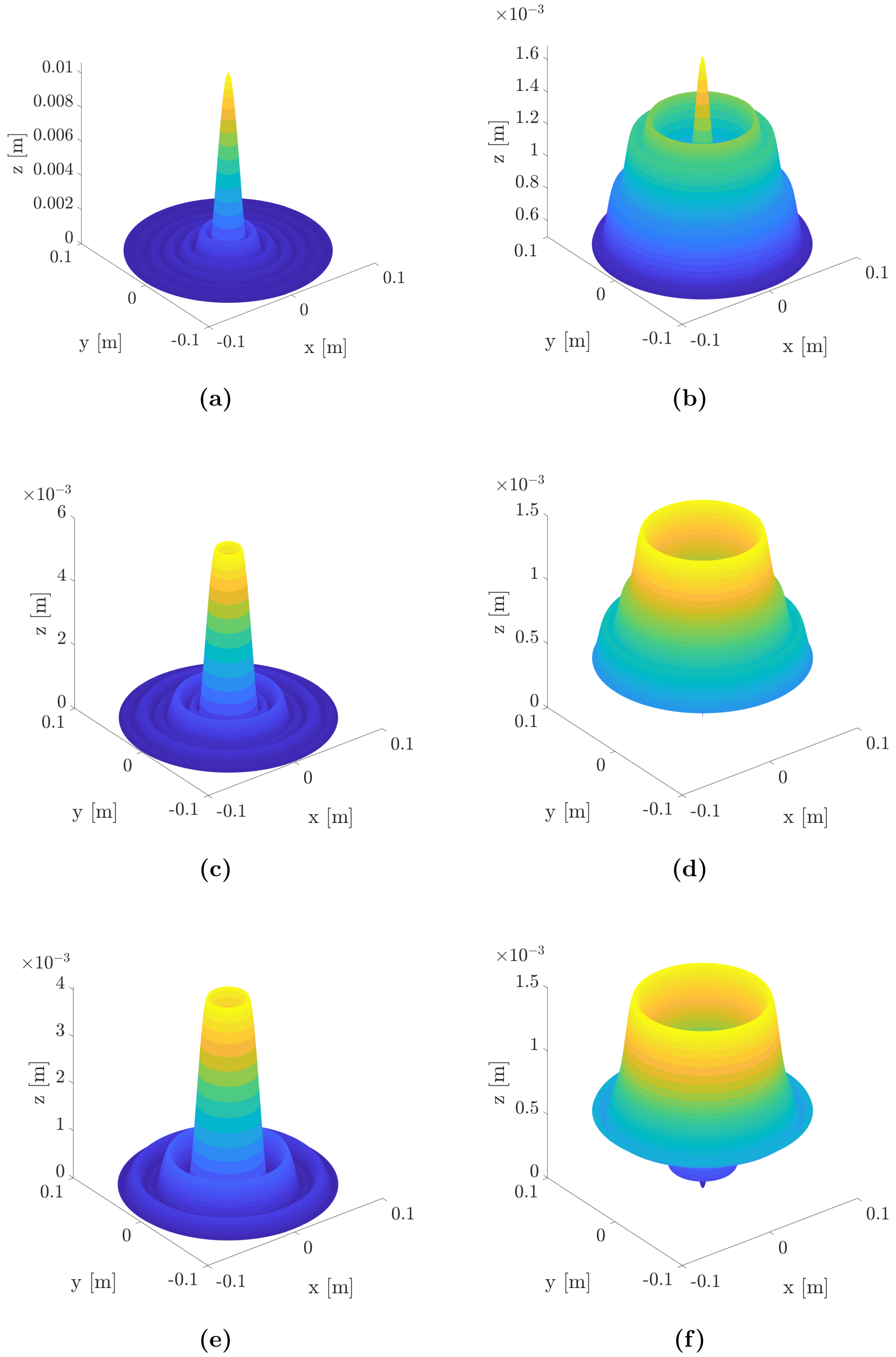

**Figure 5.6:** *Three-dimensional illustration of the various OAM field components* $\psi^{(n)}(\rho_R, \varphi_R, z)$ *with focusing (left column) and without focusing (right column) for* $\ell_n$ *values corresponding to* (a)-(b) $\ell_n = 0$, (c)-(d) $\ell_n = \pm 1$, *and* (e)-(f) $\ell_n = \pm 2$ *at* $D = 30$.

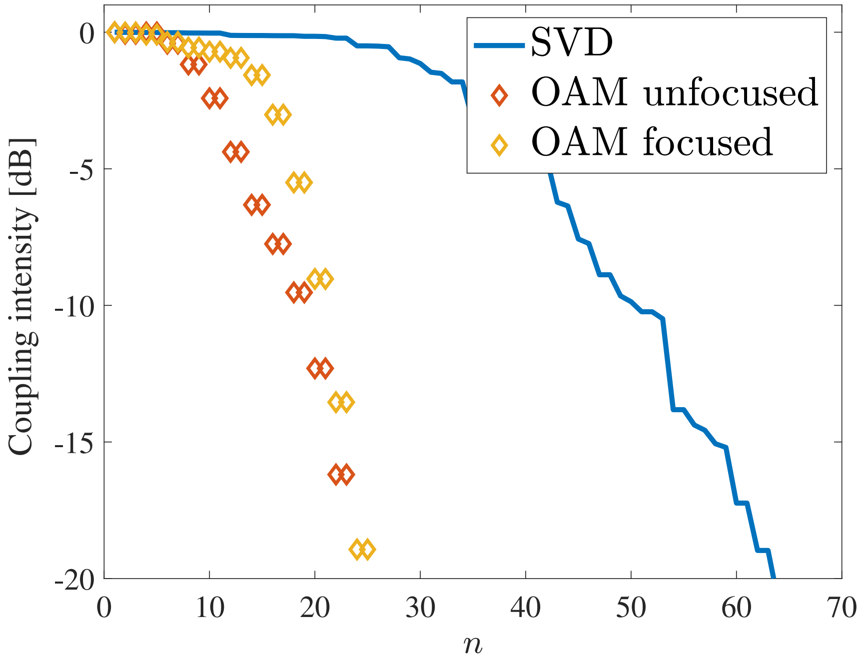

**Figure 5.7:** *Normalized coupling intensity for the unfocused and focused (at the transmitter side) OAM-based communication in comparison with coupling intensity of optimum communication modes (SVD) ($D = 50$).*

munication mode, about 40 communication modes are obtained with SVD; differently, only 10 can be exploited with OAM and about 18 with OAM using focusing at the transmitting LIS. Therefore, it is evident that the number of parallel channels is lower than that corresponding to the optimum strategy. However, system complexity is significantly reduced with respect to the optimal SVD approach. In particular, the coupling intensity obtained for focused OAM-based communication modes with low topological charge could be anyhow acceptable for certain applications, so this could be reasonably exploited for enhancing the link capacity with small additional complexity.

In Figure 5.8, the number of modes $N$ is reported as a function of the distance parameter $D$, considering $R = T = 10$. For comparison, the number of communication modes obtained from (2.14), i.e. Equation (5.1), is hereby reported.

$$N = \frac{\pi^2 R^2 T^2}{D^2} \tag{5.1}$$

Note that $N$ depends on geometrical quantities only, which are in turn reported to the wavelength. In addition, the number of modes obtained considering the significative singular values of SVD is reported. In all the cases, a threshold of $-5\,\mathrm{dB}$ is considered to determine the number of well-coupled modes.
As expected, regardless of the adopted strategy, the modes' number abruptly diminishes for increasing distance, progressively approaching the unit (far-field

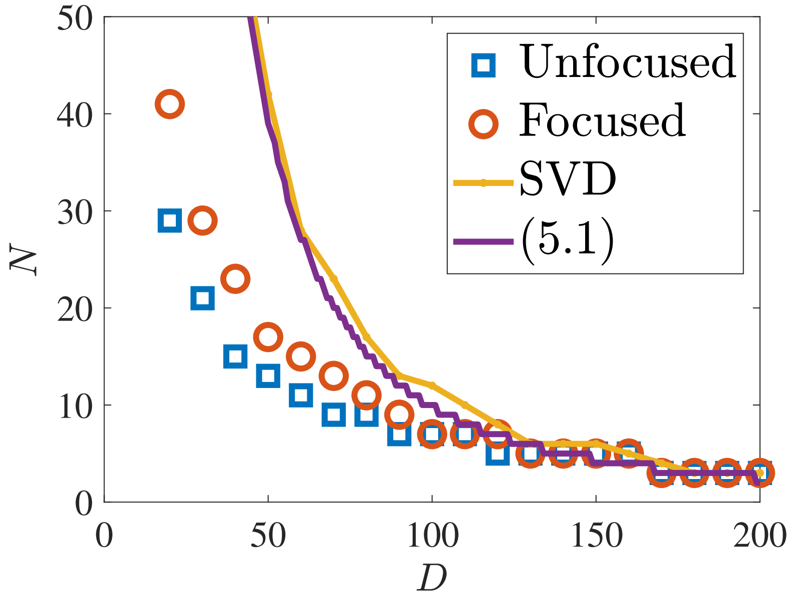

**Figure 5.8:** *Number of modes as a function of the link distance $D$ (multiples of $\lambda$). Transmitting and receiving antennas of the same size ($R = T = 10$).*

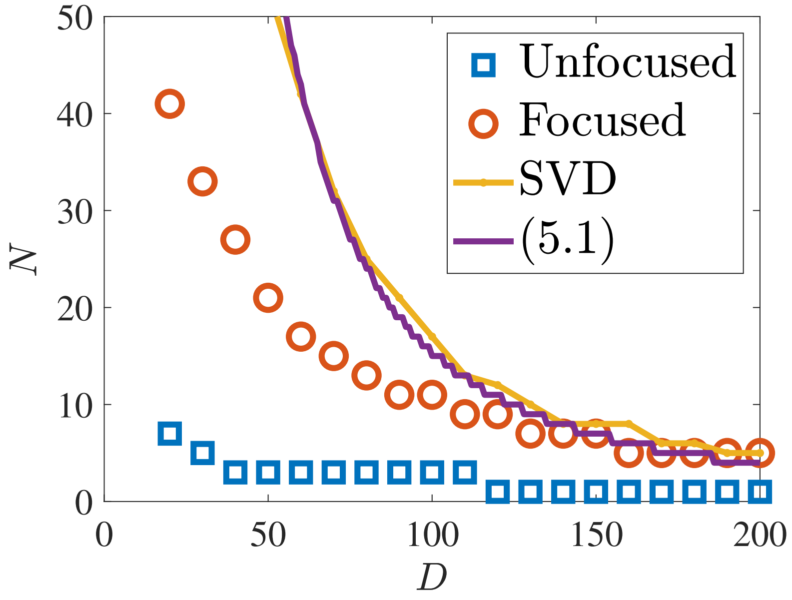

**Figure 5.9:** *Number of modes as a function of the link distance $D$ (multiples of $\lambda$). Downlink case ($R = 5, T = 25$).*

limit). The number of modes corresponding to significant singular values from SVD is very well predicted by (5.1).

Although the usage of focused OAM beams produces a greater amount of well-coupled modes, both the focused and unfocused OAM transmissions exhibit, in any case, an inferior performance compared to the optimal communication modes when the distance becomes small. Differently, when the geometrical

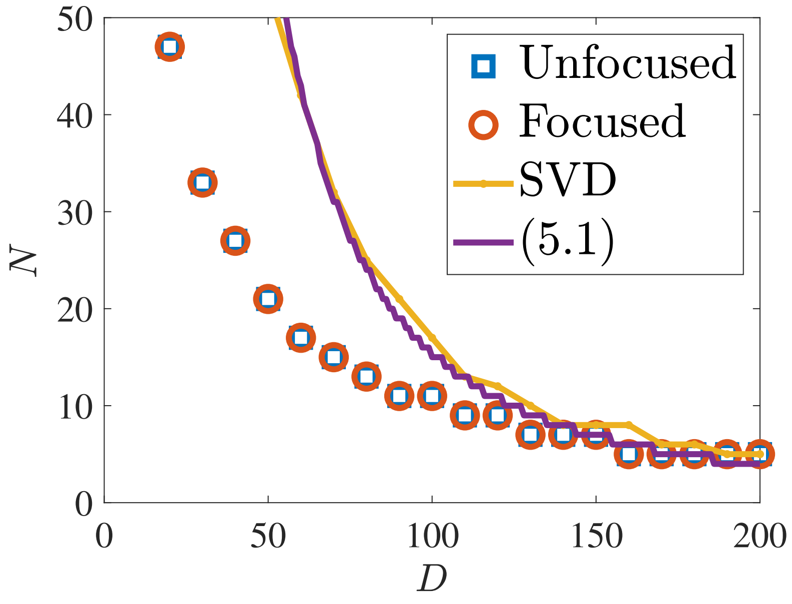

**Figure 5.10:** *Number of modes as a function of the link distance $D$ (multiples of $\lambda$). Uplink case ($R = 25, T = 5$).*

setting cannot lead to a large number of modes (e.g., for larger distances), OAM represents a viable solution to exploit channel diversity, with limited additional complexity and without the need of performing SVD.

Furthermore, the following plots show similar results when the size of the LISs greatly differs. In particular, in Figure 5.9 LIS antennas with $R = 5$ and $T = 25$ are considered. Since the transmitting antenna is much larger than the receiving one, we refer to this case as downlink transmission.
Thanks to the large dimension of the transmitting LIS, high focusing gain can be obtained, thus drastically increasing the number of well-coupled OAM-based channels. Differently, if focusing is not adopted in this downlink case, the detrimental effect of beam divergence, exasperated by the large transmitting aperture, makes OAM-based strategies quite ineffective.

The opposite case, corresponding to $R = 25$ and $T = 5$ (i.e., uplink case) is reported in Figure 5.10. In this case, the number of modes obtained with SVD or corresponding to (5.1) is clearly equivalent to that from Figure 5.9, since it is related to optimum complete bases. Differently, when considering the simpler OAM-based approach, the situation is asymmetric due to beam divergence. However, in this case, since the receiving LIS is large enough to properly collect the energy for increasing values of the topological charge, a large number of OAM-based channels can be realized, thus making the approach very appealing. On the other hand, focusing the beam at the transmitter side does not bring advantages due to the reduced size of the transmitting LIS.

Finally, Figure 5.11 illustrates the results obtained when the sub-optimum -

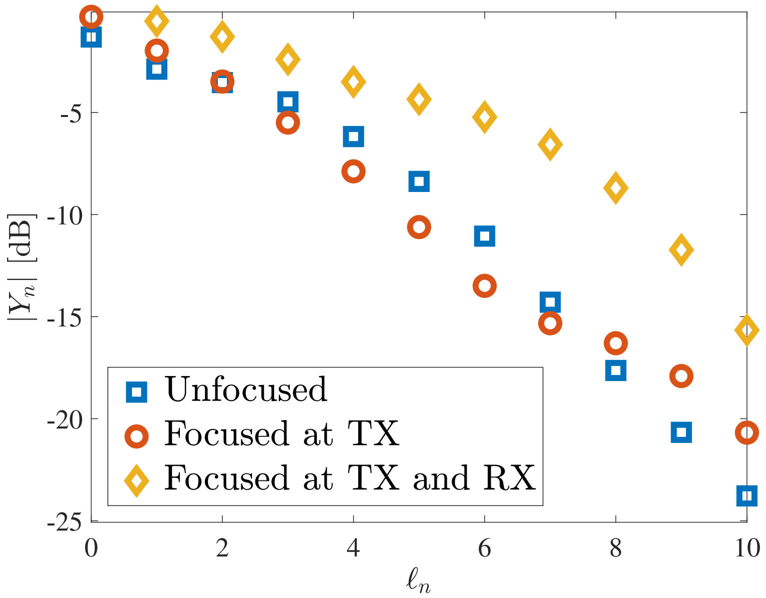

**Figure 5.11:** *Coupling for the topological charge $\ell_n$ considering the sub-optimum detection strategy based on accumulation.*

but lower complexity - detection strategy based on accumulation is considered according to (4.26). In particular, the absolute value of the decision variable $Y_n$ is reported as a function of the topological charge $\ell_n$.
Square markers correspond to the accumulation performed considering the unfocused EM field. Differently, circle markers report the effect of focusing at the transmitter side only, which is not particularly effective with such a sub-optimum scheme. In contrast, when focusing is considered at both the transmitter and receiver side, thus compensating for the quadratic phase terms of both ends, a significant improvement in the performance can be obtained.

## 5.4 Performance in AWGN

In this section, a system-level analysis is reported with the primary aim of characterizing the OAM-based communication scheme from an information-theoretical perspective by the means of a traditional performance metric as the BER. Specifically, we will focus on the system performance when the matched filter detection scheme is employed, and the initial geometrical configuration is contemplated, that is, the one corresponding to $R = T = 10$ and $D = 30$.
Although it would be of great interest and utility to investigate the analogous curves for the other simpler detection schemes, we shall here restrict our numerical study to the optimal scheme only due to software implementation concerns. Indeed, the simulation of the other two sub-optimum strategies requires an ad-hoc solution to compute the numerical integral that corresponds to the correlation operation since it requires a different processing along the

radial and the azimuthal field's components. Moreover, it should be noted that the conversion from Cartesian coordinates to polar ones is a non-linear transformation, thus the generation of the i.i.d. noise samples would require the knowledge of the bivariate AWGN noise distribution as a function of $\rho_{\mathrm{R}}$ and $\varphi_{\mathrm{R}}$ or, equivalently, an effective mapping method (e.g., by exploiting affine transformations) that allows implementing a change of variable via MATLAB code easily. Unfortunately, this requires an in-depth examination that is still under development and will thus be presented in subsequent works.

In light of this, Figure 5.12 depicts the BER of an uncoded transmission on an AWGN channel, resulting from a Monte Carlo simulation, as a function of the SNR for various $\ell_n$ values when focusing is performed at the transmitter side. Moreover, numerical results are compared with the theoretical bit error probability formula, i.e., Equation (4.21), whose outcomes are reported via red square markers.

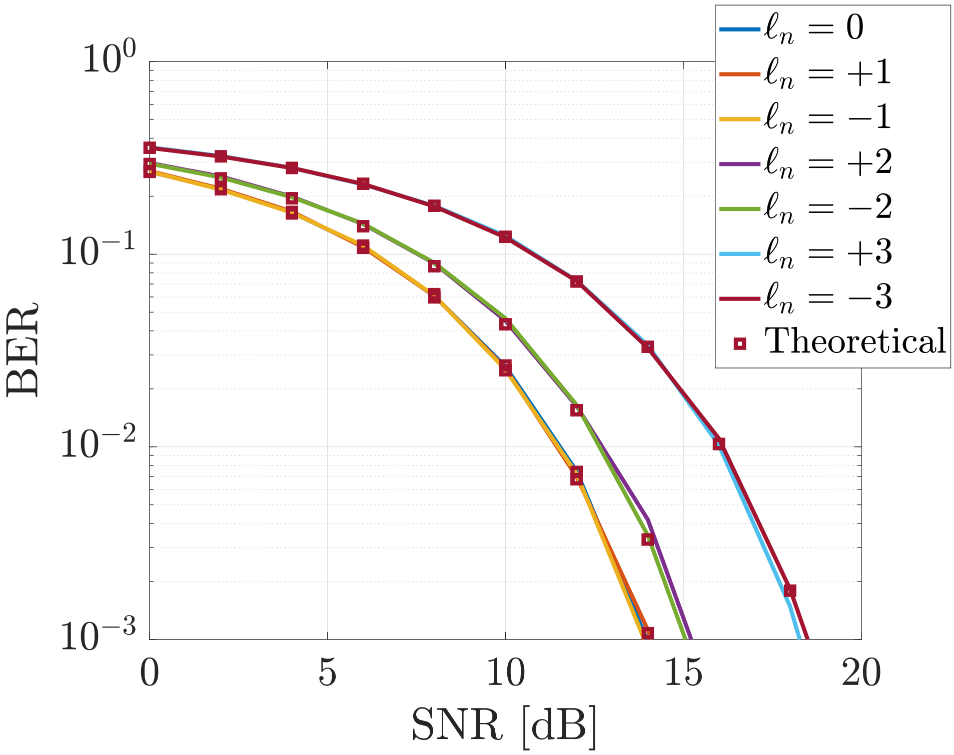

**Figure 5.12:** *BER as a function of the SNR for the matched filter detection scheme and different $\ell_n$ values. Focusing is performed at the transmitter side.*

It can be easily noticed that the simulated results are in accordance with the theoretical ones and that the curves related to the OAM modes well interpolate the trajectories identified by the square markers. In addition, emerges anew the symmetry between modes with the same absolute value of the topological charge $\ell_n$ but with opposite sign, hence displaying almost equivalent error rates for given SNR values. Notably, for increasing $\ell_n$ values, system performance rapidly degrades, and the reason for this outcome is once again determined by the presence of beam divergence, though partially compensated by focusing. Moreover, due to the specific processing performed by the matched filter at EM level, the main advantages and performance improvements are obtained when focusing takes place at the transmitting LIS, effectively counteracting the OAM beams' spreading. For this reason, we will not present the analogous BER curves when focusing is performed at the receiver side, being exactly equal to the graphs reported herein.

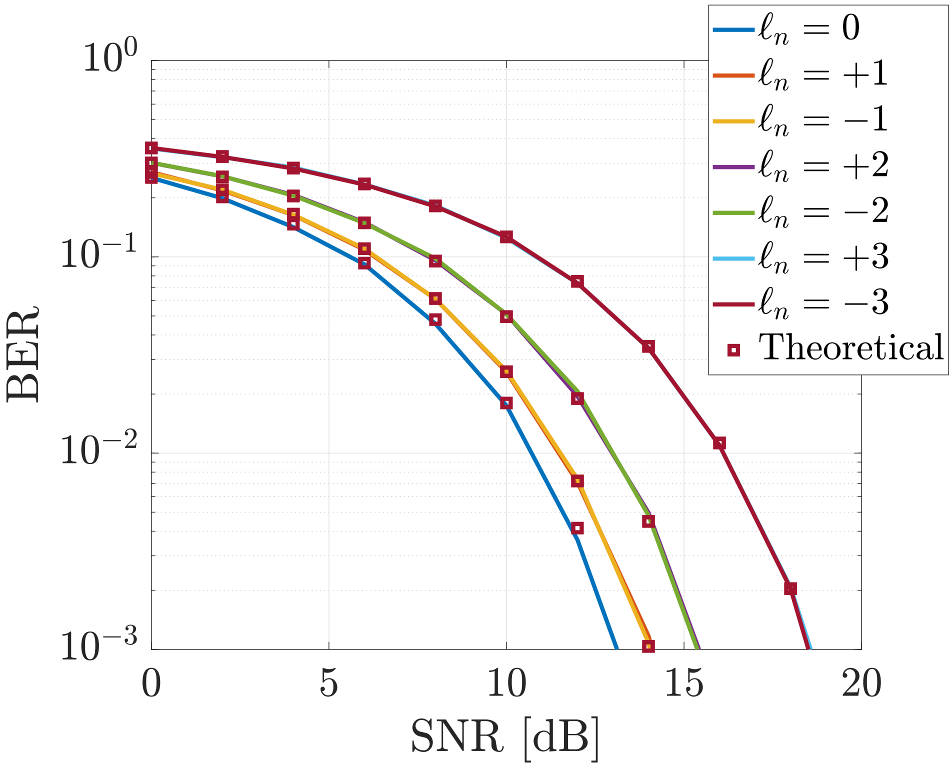

**Figure 5.13:** *BER as a function of the SNR for the matched filter detection scheme, for different $\ell_n$ values, and in the absence of focusing.*

Figure 5.13 instead reports the bit error probability for the same system configuration, but this time in the complete absence of focusing. It is evident how the performance degradation affects all the transmitted modes, particularly those with lower OAM orders. Again, the cause has to be found in the divergence phenomenon, which spreads a great fraction of the useful modes' energy away from the receiving antenna center, thus leading to a larger amount of bits that are erroneously detected.

In addition, being in turn the SNR a function of the link distance $z$, we will illustrate hereafter the BER performance of the various OAM modes for increasing link distances. This is a further result that highlights how the specific system configuration plays a crucial role not only in determining the number of communication modes at disposal and their coupling strength but also how a slight change in the distance among the antennas can lead to a severe worsening of the detector's accuracy.

Figure 5.14 reports the BER curves against the link distance (expressed as multiples of $\lambda$) when focusing is employed at the transmitter. A reference value for the SNR perceived at a distance equal to $z = 10\lambda$ has been set equal to 12 dB.
Figure 5.15 instead depicts the same graph but when in the absence of focusing. The error probability grows exponentially as the $z$ extends, being their relationship defined by the well-known free-space path loss deriving from the Friis transmission formula. Unsurprisingly, by spacing apart the LISs of a few tens of wavelengths more, the error rates rise by more than two orders of magnitude, and this effect is even intensified when no countermeasures to beams' widening are adopted.

## 5.5 Discussion

To summarize, the previous sections highlighted how the exploitation of the OAM property has both practical advantages and ineluctable disadvantages. Concerning the benefits of the OAM utilization, it has been shown that this transmission technique allows multi-modal communications, hence enabling MIMO-like LOS communication. Specifically, the basis functions proposed in (4.1) introduce the possibility of performing spatial multiplexing with a considerably lower complexity with respect to the SVD case or the usage of the CPSFs.
What is more, OAM does not only offer some benefits in terms of ease of implementation, but it is also an insensitive method to link distance variations. In other words, with both the optimal SVD approach and the beam-focusing one, the basis functions depend on the overall system geometry and need to be recomputed every time the link distance varies; with OAM waves instead, the choice of the basis sets is fixed and is not related to the system configuration. Notably, another advantage of the OAM approach is that OAM signals reception and demodulation are intrinsically simpler than the traditional demodulation of MIMO signals performed through digital signal processing (DSP). This property is due to the spatial orthogonality of OAM modes, which allows to perform signals' demodulation at EM level directly, and this is particularly profitable for wideband, mmWaves, or THz-based communications.
In addition to this, the introduction of focusing is particularly favorable for OAM propagation since it permits a significant increase in the DoFs of the OAM-based communication.

Apart from these considerations, an element of fundamental importance that is worth to be mentioned is the employment of LISs antennas rather than UCAs. In fact, the usage of large aperture antennas permits the correct reception of the multi-modal OAM signal without the need to adjust the array radius in order to be suitably collimated with the transmitted beam. Clearly, being the beam radius variable and dependent on the specific topological charge, it

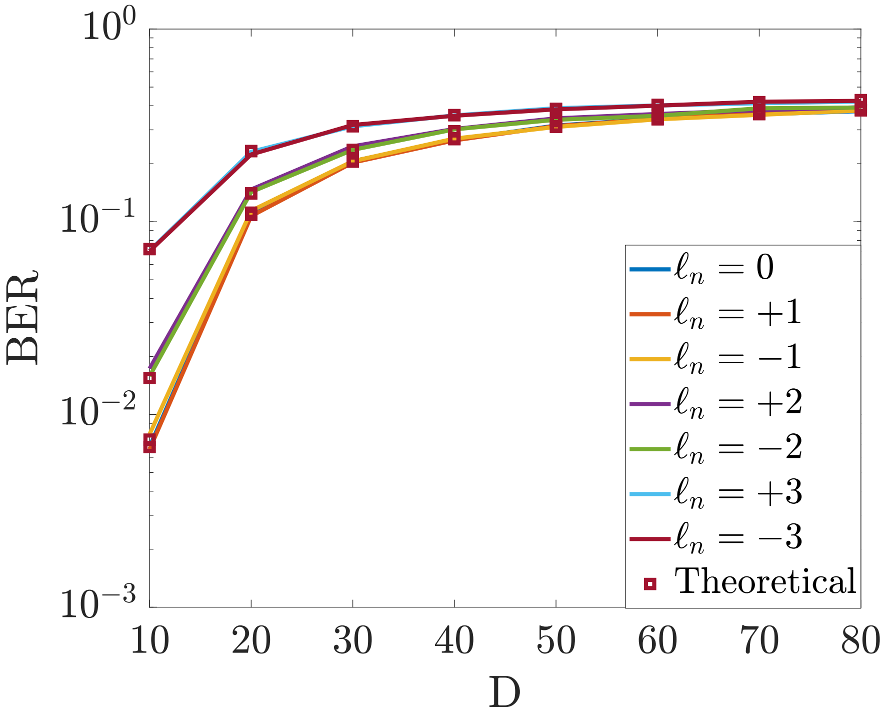

**Figure 5.14:** *BER as a function of the link distance D for the matched filter detection scheme, for different $\ell_n$ values. Focusing is performed at the transmitter side.*

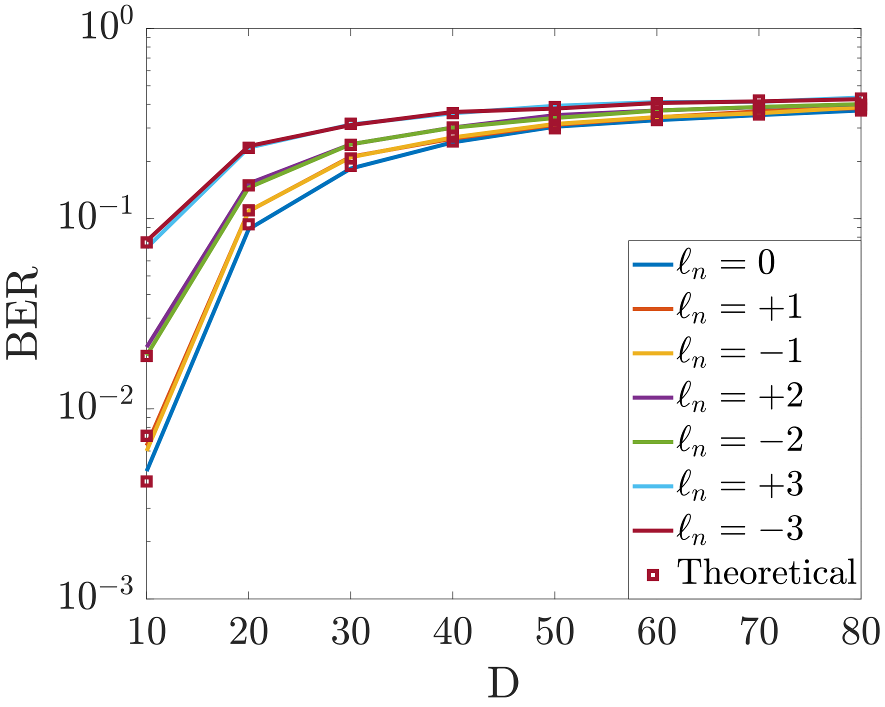

**Figure 5.15:** *BER as a function of the link distance D for the matched filter detection scheme, for different $\ell_n$ values, and in the absence of focusing.*

is impracticable with UCAs to have a unique antenna structure that suits all the available types of OAM beams.

Be that as it may, OAM communications also display several, not negligible negative aspects that necessarily need to be considered. Figure 5.7 highlighted that the number of the effectively well-coupled OAM modes is much smaller with respect to the optimum SVD case, both in the presence of focusing or not. This evidently results in the absence of any relevant channel capacity improvements with respect to traditional non-OAM communications, hence leading to a sub-optimal transmission technique. Focusing has been shown to compensate for this OAM deficiency partially. However, the focusing approach once again necessitates the exact knowledge of system geometry, which clearly implies some constraints.
Supplementary reception techniques and expedients, such as smart integration and the others we have analyzed so far, can only partially counteract the irremovable propagation phenomena, hence resulting in BER outcomes and overall performance that are certainly not superior to that of many other complex transmission techniques available nowadays.

Behind all that, it must be reminded that the considered system contemplates a paraxial, LOS, perfectly aligned scenario. Any misalignment between the transmitter and the receiver, i.e., the presence of lateral displacements or receiver angular errors, or multipath propagation results in significant power loss and crosstalk interference at the receiver side and, at its extreme, in the complete loss of information, hence leading to an unavoidable failure of the OAM-based approaches if no proper strategies to cope with such effects are considered. Lastly, when non-paraxial propagation is considered, OAM-based transmissions again require the exact knowledge of the link distance and the information related to antennas' orientation.

# Chapter 6

# Conclusion

This dissertation discussed OAM-based holographic MIMO communications exploiting large intelligent surfaces as antennas.
Starting from the description of beams in terms of communication modes, simple OAM-related basis functions at the transmitter and receiver sides have been investigated. In addition, different detection strategies to be adopted at the receiver side have been analyzed in detail.
The numerical study has shown the actual possibility of having a considerable number of orthogonal OAM channels, particularly when focusing is exploited to limit the beam divergence characteristic of OAM beams within the near field. Nevertheless, no significant channel capacity achievements can be obtained with respect to alternative but more complex strategies.
Although the exploitation of beam focusing resulted in being beneficial for OAM waves propagation, also the joint OAM-focusing approach is still far from being optimum, especially in light of the paraxial, perfectly aligned scenario that is required for ideal OAM helices propagation.
Therefore, we can conclude that OAM modes constitute a particular choice of communication modes, i.e., an alternative basis set, which is sub-optimum with respect to the optimum basis functions derived from the SVD approach.

To conclude, this thesis work could be considered a first starting point for further developments and applications.
To mention some interesting perspectives that may be considered, future works could be targeted to the complete description of the EM field as a complex vector, in that way increasing the number of DoFs at disposal.
Furthermore, more efficient algorithms for the smart integration procedure could be investigated, together with the optimization of its threshold as a function of the specific OAM mode to be detected and the SNR, e.g., so that to maximize the energy collected by the strongest, lower order OAM modes.
In addition, the decision threshold for the energy detection scheme could be improved by implementing a heuristic computing method that takes into account the number of DoFs available, the fraction of energy that is allocated to each OAM mode, the noise variance, and other parameters.
Likewise, identifying an accurate noise model that considers the spatial cor-

relation of the various points on the receiving antenna surface might be of great utility in rendering our theoretical model as realistic as possible. In particular, manifold aspects and adverse physical effects related to the specific technologies adopted to create LIS antennas (e.g., metamaterials and ad-hoc electronics) might also be considered, thus requiring the adoption of a multidisciplinary approach.

Lastly, another interesting advancement that could be explored is the system design and EM propagation study for specific applications based on near-field OAM multiplexing, e.g., for indoor environments or dynamic industrial scenarios.

# List of Figures

2.1 Smart radio environment with a LIS antenna communicating with multiple users, both in the near and far fields, eventually assisted by intelligent reflective surfaces (IRSs) [4]. . . . . . . . . 4
2.2 Schematic representation of communication modes between a couple of LIS antennas. . . . . . . . . . . . . . . . . . . . . . . . . . 7
2.3 Scenario with two LISs in paraxial conditions spaced of $z$. . . . 8

3.1 The illustrative distinction between the SAM (left) and OAM components (right) of the EM angular momentum. . . . . . . . 11
3.2 Plot of the propagating twisted wavefronts (left) and the phase and intensity distribution, respectively, of the OAM beams (right) for different $\ell$ values. . . . . . . . . . . . . . . . . . . . . . . . . 12
3.3 A graphic representation of the beam divergence phenomenon (a) and the possible misalignment errors (b) that can occur at the receiver side [32]. . . . . . . . . . . . . . . . . . . . . . . . . 15
3.4 Illustration of the effects of atmospheric turbulence on OAM vortexes propagation, leading to distortion and inter-modal interference [33]. . . . . . . . . . . . . . . . . . . . . . . . . . . . 15
3.5 (a) The satellite view of Venice's canal where the first OAM broadcast transmission took place. (b) Venice's Palazzo Ducale displaying the writing "signal received", after the successful reception of the OAM multiplexed signal. . . . . . . . . . . . . . . 16
3.6 Illustration of the phase interferometer utilized for Venice's experiment, composed of two connected receiving antennas connected through a 180° phase-shift cable. . . . . . . . . . . . . 17

4.1 Block diagram of the complete reception scheme in the presence of AWGN noise. . . . . . . . . . . . . . . . . . . . . . . . . . . 26
4.2 Matched filtering processing scheme for OAM detection. . . . . 28
4.3 Plot of the Bessel functions' terms included in Equation (4.26) as a function of $\rho_{\mathrm{R}}$ for different topological charges ($N = 7$). . . 31
4.4 Accumulation-based processing schemes for OAM detection. . . 31
4.5 Energy detection-based processing scheme for OAM detection. . 35

5.1 Received EM field along the radial coordinate $\rho_{\mathrm{R}}$ for different topological charges $\ell_n$ (normalized to $\max\{|f_0(\rho_{\mathrm{R}})|\}$). . . . . . . 41

5.2 Received EM field along the radial coordinate $\rho_{\mathrm{R}}$ for different topological charges $\ell_n$ using focusing at the transmitter side (normalized to $\max\{|f_0(\rho_{\mathrm{R}})|\}$). . . . . . . . . . . . . . . . . . . 42
5.3 Example of transmitting and receiving amplitude/phase profiles, with and without focusing, for $\ell_n = 0$ (first line), $\ell_n = +1$ (second line), and $\ell_n = +3$ (third line). The first and second columns refer respectively to the unfocused and focused phase profiles at the transmitter, while the third and fourth columns represent the received field amplitudes for the unfocused and focused case. The last two columns correspondingly depict the received phase profiles without and with focusing ($T = R = 5$, $D = 20$). . . . . . . . . . . . . . . . . . . . . . . . . . . . . 43
5.4 EM field distribution on the receiving LIS when focusing is performed both at the transmitter and the receiver at $D = 30$. . . . 43
5.5 Unfocused EM field distribution on the receiving LIS, with the global maximum corresponding to the fundamental mode ($\ell_n = 0$) at $D = 30$. . . . . . . . . . . . . . . . . . . . . . . . . . 44
5.6 Three-dimensional illustration of the various OAM field components $\psi^{(n)}(\rho_{\mathrm{R}}, \varphi_{\mathrm{R}}, z)$ with focusing (left column) and without focusing (right column) for $\ell_n$ values corresponding to (a)-(b) $\ell_n = 0$, (c)-(d) $\ell_n = \pm 1$, and (e)-(f) $\ell_n = \pm 2$ at $D = 30$. . . . . 45
5.7 Normalized coupling intensity for the unfocused and focused (at the transmitter side) OAM-based communication in comparison with coupling intensity of optimum communication modes (SVD) ($D = 50$). . . . . . . . . . . . . . . . . . . . . . . . 46
5.8 Number of modes as a function of the link distance $D$ (multiples of $\lambda$). Transmitting and receiving antennas of the same size ($R = T = 10$). . . . . . . . . . . . . . . . . . . . . . . . . 47
5.9 Number of modes as a function of the link distance $D$ (multiples of $\lambda$). Downlink case ($R = 5, T = 25$). . . . . . . . . . . . . . . 47
5.10 Number of modes as a function of the link distance $D$ (multiples of $\lambda$). Uplink case ($R = 25, T = 5$). . . . . . . . . . . . . . . . 48
5.11 Coupling for the topological charge $\ell_n$ considering the sub-optimum detection strategy based on accumulation. . . . . . . . . . . . 49
5.12 BER as a function of the SNR for the matched filter detection scheme and different $\ell_n$ values. Focusing is performed at the transmitter side. . . . . . . . . . . . . . . . . . . . . . . . . . 50
5.13 BER as a function of the SNR for the matched filter detection scheme, for different $\ell_n$ values, and in the absence of focusing. . 51
5.14 BER as a function of the link distance $D$ for the matched filter detection scheme, for different $\ell_n$ values. Focusing is performed at the transmitter side. . . . . . . . . . . . . . . . . . . . . . 53
5.15 BER as a function of the link distance $D$ for the matched filter detection scheme, for different $\ell_n$ values, and in the absence of focusing. . . . . . . . . . . . . . . . . . . . . . . . . . . . 53

# Bibliography

[1] G. Gradoni, M. Di Renzo, A. Diaz-Rubio, S. Tretyakov, C. Caloz, Z. Peng, A. Alù, G. Lerosey, M. Fink, V. Galdi *et al.*, "Smart radio environments," *arXiv preprint arXiv:2111.08676*, 2021.

[2] E. Björnson, L. Sanguinetti, H. Wymeersch, J. Hoydis, and T. L. Marzetta, "Massive MIMO is a reality. What is next?: Five promising research directions for antenna arrays," *Digital Signal Processing*, vol. 94, pp. 3–20, June 2019, Special Issue on Source Localization in Massive MIMO.

[3] M. D. Renzo, M. Debbah, D.-T. Phan-Huy, A. Zappone, M.-S. Alouini, C. Yuen, V. Sciancalepore, G. C. Alexandropoulos, J. Hoydis, H. Gacanin *et al.*, "Smart radio environments empowered by reconfigurable AI meta-surfaces: An idea whose time has come," *EURASIP Journal on Wireless Communications and Networking*, vol. 2019, no. 1, pp. 1–20, May 2019.

[4] D. Dardari and N. Decarli, "Holographic communication using intelligent surfaces," *IEEE Communications Magazine*, vol. 59, no. 6, pp. 35–41, June 2021.

[5] M. Di Renzo, A. Zappone, M. Debbah, M.-S. Alouini, C. Yuen, J. de Rosny, and S. Tretyakov, "Smart radio environments empowered by reconfigurable intelligent surfaces: How it works, state of research, and the road ahead," *IEEE Journal on Selected Areas in Communications*, vol. 38, no. 11, pp. 2450–2525, July 2020.

[6] S. Hu, F. Rusek, and O. Edfors, "Beyond Massive MIMO: The potential of data transmission with large intelligent surfaces," *IEEE Transactions on Signal Processing*, vol. 66, no. 10, pp. 2746–2758, March 2018.

[7] D. Dardari, "Communicating with large intelligent surfaces: Fundamental limits and models," *IEEE Journal on Selected Areas in Communications*, vol. 38, no. 11, pp. 2526–2537, November 2020.

[8] E. Basar, M. Di Renzo, J. De Rosny, M. Debbah, M.-S. Alouini, and R. Zhang, "Wireless communications through reconfigurable intelligent surfaces," *IEEE Access*, vol. 7, pp. 116 753–116 773, August 2019.

[9] S. Tretyakov, "Metasurfaces for general transformations of electromagnetic fields," *Philosophical transactions. Series: A Mathematical, physical, and engineering sciences*, vol. 373, August 2015.

[10] A. Silva, F. Monticone, G. Castaldi, V. Galdi, A. Alù, and N. Engheta, "Performing mathematical operations with metamaterials," *Science*, vol. 343, no. 6167, pp. 160–163, January 2014.

[11] D. González-Ovejero, G. Minatti, G. Chattopadhyay, and S. Maci, "Multibeam by metasurface antennas," *IEEE Transactions on Antennas and Propagation*, vol. 65, no. 6, pp. 2923–2930, February 2017.

[12] E. Basar, M. Di Renzo, J. De Rosny, M. Debbah, M.-S. Alouini, and R. Zhang, "Wireless communications through reconfigurable intelligent surfaces," *IEEE access*, vol. 7, pp. 116 753–116 773, August 2019.

[13] D. A. Miller, "Communicating with waves between volumes: evaluating orthogonal spatial channels and limits on coupling strengths," *Applied Optics*, vol. 39, no. 11, pp. 1681–1699, April 2000.

[14] N. Decarli and D. Dardari, "Communication modes with large intelligent surfaces in the near field," *IEEE Access*, vol. 9, pp. 165 648–165 666, December 2021.

[15] J. Xu, "Degrees of freedom of OAM-based line-of-sight radio systems," *IEEE Transactions on Antennas and Propagation*, vol. 65, no. 4, pp. 1996–2008, April 2017.

[16] B. Thidé and F. Tamburini, "The physics of angular momentum radio," in *2015 1st URSI Atlantic Radio Science Conference (URSI AT-RASC)*. IEEE, May 2015, pp. 1–1.

[17] L. Allen, M. Padgett, and M. Babiker, "IV. The Orbital Angular Momentum of Light," ser. Progress in Optics, E. Wolf, Ed. Elsevier, 1999, vol. 39, pp. 291–372.

[18] R. Chen, H. Zhou, M. Moretti, X. Wang, and J. Li, "Orbital angular momentum waves: Generation, detection, and emerging applications," *IEEE Communications Surveys and Tutorials*, vol. 22, no. 2, pp. 840–868, November 2020.

[19] S. M. Barnett, "Optical angular-momentum flux," *Journal of Optics B: Quantum and Semiclassical Optics*, vol. 4, no. 2, p. S7, December 2001.

[20] K. Zhang, Y. Wang, Y. Yuan, and S. N. Burokur, "A review of orbital angular momentum vortex beams generation: from traditional methods to metasurfaces," *Applied sciences*, vol. 10, no. 3, p. 1015, February 2020.

[21] A. E. Siegman, *Lasers.* University Science Books, Mill Valley, California, 1986.

[22] C. Liu, J. Liu, L. Niu, X. Wei, K. Wang, and Z. Yang, "Terahertz circular Airy vortex beams," *Scientific reports*, vol. 7, no. 1, pp. 1–8, June 2017.

[23] R. Kadlimatti and P. V. Parimi, "Millimeter-wave nondiffracting circular Airy OAM beams," *IEEE Transactions on Antennas and Propagation*, vol. 67, no. 1, pp. 260–269, October 2018.

[24] J. Wang, J.-Y. Yang, I. Fazal, N. Ahmed, Y. Yan, H. Huang, Y. Ren, Y. Yue, S. Dolinar, M. Tur, and A. E. Willner, "Terabit free-space data transmission employing orbital angular momentum multiplexing," *Nature Photonics*, vol. 6, pp. 488–496, June 2012.

[25] W. Cheng, W. Zhang, H. Jing, S. Gao, and H. Zhang, “Orbital angular momentum for wireless communications,” *IEEE Wireless Communications*, vol. 26, no. 1, pp. 100–107, December 2018.

[26] L. Liang, W. Cheng, H. Zhang, Z. Li, and Y. Li, “Orbital-angular-momentum based mode-hopping: A novel anti-jamming technique,” in *2017 IEEE/CIC International Conference on Communications in China (ICCC)*, October 2017, pp. 1–6.

[27] W. Cheng, H. Zhang, L. Liang, H. Jing, and Z. Li, “Orbital-angular-momentum embedded massive MIMO: Achieving multiplicative spectrum-efficiency for mmwave communications,” *IEEE Access*, vol. 6, pp. 2732–2745, December 2017.

[28] Z. Zhang, S. Zheng, W. Zhang, X. Jin, H. Chi, and X. Zhang, “Experimental demonstration of the capacity gain of plane spiral OAM-based MIMO system,” *IEEE Microwave and Wireless Components Letters*, vol. 27, no. 8, pp. 757–759, July 2017.

[29] Y. Yan, L. Li, G. Xie, M. Ziyadi, A. M. Ariaei, Y. Ren, O. Renaudin, Z. Zhao, Z. Wang, C. Liu, S. Sajuyigbe, S. Talwar, S. Ashrafi, A. F. Molisch, and A. E. Willner, “OFDM over mm-wave OAM channels in a multipath environment with intersymbol interference,” in *2016 IEEE Global Communications Conference (GLOBECOM)*, December 2016, pp. 1–6.

[30] T. Yuan, H. Wang, Y. Qin, and Y. Cheng, “Electromagnetic vortex imaging using uniform concentric circular arrays,” *IEEE Antennas and Wireless Propagation Letters*, vol. 15, pp. 1024–1027, October 2015.

[31] E. Mari, F. Spinello, M. Oldoni, R. A. Ravanelli, F. Romanato, and G. Parisi, “Near-field experimental verification of separation of OAM channels,” *IEEE Antennas and Wireless Propagation Letters*, vol. 14, pp. 556–558, November 2015.

[32] G. Xie, L. Li, Y. Ren, H. Huang, Y. Yan, N. Ahmed, Z. Zhao, M. P. J. Lavery, N. Ashrafi, S. Ashrafi, R. Bock, M. Tur, A. F. Molisch, and A. E. Willner, “Performance metrics and design considerations for a free-space optical orbital-angular-momentum-multiplexed communication link,” *Optica*, vol. 2, no. 4, pp. 357–365, April 2015.

[33] M. Krenn, R. Fickler, M. Fink, J. Handsteiner, M. Malik, T. Scheidl, R. Ursin, and A. Zeilinger, “Communication with spatially modulated light through turbulent air across Vienna,” *New Journal of Physics*, vol. 16, no. 11, p. 113028, November 2014.

[34] Y. Zhang, W. Feng, and N. Ge, “On the restriction of utilizing orbital angular momentum in radio communications,” *2013 8th International Conference on Communications and Networking in China (CHINACOM)*, pp. 271–275, August 2013.

[35] F. Tamburini, E. Mari, A. Sponselli, F. Romanato, B. Thidé, A. Bianchini, L. Palmieri, and C. Someda, “Encoding many channels on the same frequency through radio vorticity: First experimental test,” *New Journal of Physics*, vol. 14, p. 033001, April 2012.

[36] M. Tamagnone, C. Craeye, and J. Perruisseau-Carrier, “Comment on ‘encoding many channels on the same frequency through radio vorticity: first experimental test’,” *New Journal of Physics*, vol. 14, no. 11, p. 118001, November 2012.

[37] F. Tamburini, B. Thidé, E. Mari, A. Sponselli, A. Bianchini, and F. Romanato, “Reply to comment on ‘encoding many channels on the same frequency through radio vorticity: first experimental test’,” *New Journal of Physics*, vol. 14, no. 11, p. 118002, November 2012.

[38] M. Tamagnone, C. Craeye, and J. Perruisseau-Carrier, “Comment on ‘reply to comment on “encoding many channels on the same frequency through radio vorticity: first experimental test” ’,” *New Journal of Physics*, vol. 15, no. 7, p. 078001, July 2013.

[39] F. Tamburini, E. Mari, G. Parisi, F. Spinello, M. Oldoni, R. Ravanelli, P. Coassini, C. Someda, B. Thidé, and F. Romanato, “Tripling the capacity of a point-to-point radio link by using electromagnetic vortices,” *Radio Science*, vol. 50, pp. 1–8, 06 2015.

[40] O. Edfors and A. J. Johansson, “Is orbital angular momentum (OAM) based radio communication an unexploited area?” *IEEE Transactions on Antennas and Propagation*, vol. 60, no. 2, pp. 1126–1131, October 2011.

[41] Z. Zhang, S. Zheng, W. Zhang, X. Jin, H. Chi, and X. Zhang, “Experimental demonstration of the capacity gain of plane spiral OAM-based MIMO system,” *IEEE Microwave and Wireless Components Letters*, vol. 27, no. 8, pp. 757–759, July 2017.

[42] H. Jing, W. Cheng, X.-G. Xia, and H. Zhang, “Orbital-angular-momentum versus MIMO: Orthogonality, degree of freedom, and capacity,” in *2018 IEEE 29th Annual International Symposium on Personal, Indoor and Mobile Radio Communications (PIMRC).* IEEE, September 2018, pp. 1–7.

[43] D. A. Miller, “Waves, modes, communications, and optics: a tutorial,” *Advances in Optics and Photonics*, vol. 11, no. 3, pp. 679–825, September 2019.

[44] S. M. Mohammadi, L. K. S. Daldorff, J. E. S. Bergman, R. L. Karlsson, B. Thide, K. Forozesh, T. D. Carozzi, and B. Isham, “Orbital angular momentum in radio—a system study,” *IEEE Transactions on Antennas and Propagation*, vol. 58, no. 2, pp. 565–572, February 2010.

[45] P. Nepa and A. Buffi, “Near-field-focused microwave antennas: Near-field shaping and implementation.” *IEEE Antennas and Propagation Magazine*, vol. 59, no. 3, pp. 42–53, April 2017.

[46] E. Björnson, Ö. T. Demir, and L. Sanguinetti, “A primer on near-field beamforming for arrays and reconfigurable intelligent surfaces,” in *2021 55th Asilomar Conference on Signals, Systems, and Computers*, November 2021, pp. 105–112.

[47] C. Balanis, *Antenna Theory: Analysis and Design.* Wiley, 2015.

[48] A. de Jesus Torres, L. Sanguinetti, and E. Björnson, “Electromagnetic interference in RIS-aided communications,” *IEEE Wireless Communications Letters*, vol. 11, no. 4, pp. 668–672, November 2022.

[49] E. Björnson and L. Sanguinetti, "Rayleigh fading modeling and channel hardening for reconfigurable intelligent surfaces," *IEEE Wireless Communications Letters*, vol. 10, no. 4, pp. 830–834, December 2021.

[50] P. Massoud Salehi and J. Proakis, *Digital Communications.* McGraw-Hill Education, 2007.

[51] Y. C. Eldar, A. V. Oppenheim, and D. Egnor, "Orthogonal and projected orthogonal matched filter detection," *Signal Processing*, vol. 84, no. 4, pp. 677–693, April 2004.

[52] N. Decarli, A. Giorgetti, D. Dardari, M. Chiani, and M. Z. Win, "Stop-and-go receivers for non-coherent impulse communications," *IEEE Transactions on Wireless Communications*, vol. 13, no. 9, pp. 4821–4835, July 2014.

[53] N. Decarli, A. Giorgetti, D. Dardari, and M. Chiani, "Blind integration time determination for UWB transmitted reference receivers," in *2011 IEEE Global Telecommunications Conference-GLOBECOM 2011.* IEEE, 2011, pp. 1–5.

[54] H. Urkowitz, "Energy detection of unknown deterministic signals," *Proceedings of the IEEE*, vol. 55, no. 4, pp. 523–531, April 1967.

[55] A. Goldsmith, *Wireless Communications.* Cambridge University Press, 2005.

[56] P. Humblet and M. Azizoglu, "On the bit error rate of lightwave systems with optical amplifiers," *Journal of Lightwave Technology*, vol. 9, no. 11, pp. 1576–1582, November 1991.

[57] S. Paquelet, L.-M. Aubert, and B. Uguen, "An impulse radio asynchronous transceiver for high data rates," in *2004 International Workshop on Ultra Wideband Systems Joint with Conference on Ultra Wideband Systems and Technologies. Joint UWBST-IWUWBS 2004*, May 2004, pp. 1–5.

# Ringraziamenti